

Multiwavelength Monitoring of the Narrow-Line Seyfert 1 Galaxy Akn 564. II. Ultraviolet Continuum and Emission-line Variability

S. Collier,¹ D.M. Crenshaw,² B.M. Peterson,¹ W.N. Brandt,³ J. Clavel,⁴ R. Edelson,^{5,6} I.M. George,^{7,8} K. Horne,^{9,10} G.A. Kriss,¹¹ S. Mathur,¹ H. Netzer,¹² P.T. O'Brien,⁶ R.W. Pogge,¹ K.A. Pounds,⁶ P. Romano,¹ O. Shemmer,¹² T.J. Turner,^{7,8} and W. Wamsteker⁴

ABSTRACT

We present results of an intensive two-month campaign of approximately daily spectrophotometric monitoring of the narrow-line Seyfert 1 galaxy Akn 564 with the *Hubble Space Telescope (HST)*. The fractional variability amplitude of the continuum variations between 1365–3000 Å is $\sim 6\%$, about a factor 3 less than that found in typical Seyfert 1 galaxies over a similar period of time. However, large amplitude, short time-scale flaring behavior is evident, with trough-to-peak flux changes of about 18% in approximately 3 days. We present evidence for wavelength-dependent continuum time delays, with the variations at 3000 Å lagging behind those at 1365 Å by about 1 day. These delays may be interpreted as evidence for a stratified continuum reprocessing region, possibly an accretion-disk structure. The Ly α $\lambda 1216$ emission-line exhibits flux variations of about 1% amplitude. These variations lag those at 1365 Å by $\lesssim 3$ days, and combining this with the line width yields a virial black-hole mass limit of $\lesssim 8 \times 10^6 M_\odot$. We caution, the low amplitude Ly α $\lambda 1216$ variations may indicate the

¹Department of Astronomy, The Ohio State University, 140 West 18th Avenue, Columbus, OH 43210.

²Catholic University of America and Laboratory for Astronomy and Solar Physics, NASA Goddard Space Flight Center, Code 681, Greenbelt, MD 20771

⁵Department of Astronomy & Astrophysics, The Pennsylvania State University, 525 Davey Laboratory, University Park, PA 16802

⁴ESA, P.O. Box 50727, 28080 Madrid, Spain

⁵Department of Physics and Astronomy, University of California, Los Angeles, CA 90095-1562

⁶Department of Physics and Astronomy, University of Leicester, University Road, Leicester, LE1 7RH, UK

⁷Joint Center for Astrophysics, Department of Physics, University of Maryland, Baltimore County, 1000 Hilltop Circle, Baltimore, MD 21250

⁸Laboratory for High Energy Astrophysics, Code 660, NASA/Goddard Space Flight Center, Greenbelt, MD 20771

⁹School of Physics and Astronomy, University of St. Andrews, St. Andrews, KY16 9SS, UK

¹⁰Department of Astronomy, University of Texas, Austin, TX 78704

¹¹Space Telescope Science Institute, 3700 San Martin Drive, Baltimore, MD 21218

¹²School of Physics and Astronomy and the Wise Observatory, The Raymond and Beverly Sackler Faculty of Exact Sciences, Tel Aviv University, Tel Aviv 69978, Israel

bulk of the emission region is at larger radii. This scenario affects the veracity of our black hole mass upper limit in an uncertain manner due to the unknown nature of the gas velocity field. Our mass estimate is thus unreliable, however, it is consistent with the independent estimate $M \sim 1 \times 10^7 M_\odot$ of Pounds et al. (2001), based on a fluctuation power spectrum analysis of X-ray variability in Akn 564. The black-hole mass and 5100 Å luminosity of Akn 564 are consistent with the hypothesis that, relative to Seyfert 1 galaxies, NLS1s have lower black hole masses and higher accretion rates. Other strong emission lines, e.g., C IV $\lambda 1549$ and He II $\lambda 1640$, are constrained to vary with amplitudes of $< 5\%$. This low-level of emission-line variability is different from most Seyfert 1 galaxies, which characteristically display variations of $\sim 10\%$ on similar time scales.

Subject headings: galaxies: individual (Akn 564) — galaxies: active — galaxies: Seyfert — Accretion discs

1. Introduction

Narrow-line Seyfert 1 (NLS1) galaxies were first classified on the basis of their narrow permitted optical emission lines, with $H\beta$ full-width-half-maximum (FWHM) $\lesssim 2000 \text{ km s}^{-1}$ (Osterbrock & Pogge 1985). They also exhibit distinctive X-ray properties (e.g., Puchnarewicz et al. 1992; Boller et al. 1996; Brandt, Mathur, & Elvis 1997; Turner 1999; Leighly 1999a, b). These include a steep soft excess with photon index $\Gamma_{\text{soft}} > 3$ (photon flux $P_E \propto E^{-\Gamma}$), a steep hard power law with $\Gamma_{\text{hard}} > 2.5$, and rapid, short time-scale variations (e.g., $\sim 30\%$ in 1500 sec). Their UV/optical properties place them at one extreme of the Boroson & Green (1992) primary eigenvector that has been identified in a principal component analysis; specifically, NLS1 classification correlates with strong optical Fe II and weak [O III] $\lambda 5007$ emission. NLS1s are thus potentially useful in identifying the underlying physics that defines the primary eigenvector.

A number of scenarios have been posited to explain NLS1 properties:

1. NLS1s may have larger broad-line region (BLR) sizes compared to Seyfert 1 (S1) galaxies. The steeper soft excesses imply higher ionizing fluxes than S1 galaxies with comparable luminosities. Under certain conditions this may lead to larger BLR sizes and hence smaller permitted line widths, assuming they reflect virialized motions about the putative black hole (Guilbert, Fabian, & McCray 1983; Wandel & Boller 1998).
2. NLS1s may be low-inclination i , nearly face-on systems (Osterbrock & Pogge 1985). The line widths, attributable to orbital, virialized motions in a common plane are decreased by $\sin i$, and the strong soft X-ray fluxes are reconcilable with accretion disk models (e.g., Madau 1988). However, this orientation scenario has problems explaining the low [O III] luminosities often observed (e.g., Boroson & Green 1992).

3. NLS1s may have relatively low black hole masses with higher than normal accretion rates, compared to S1 galaxies (Pounds, Done, & Osborne 1995). The smaller line widths are attributable to the reduced gravitational potential in which they form, and higher accretion rates result in luminosities that are large for their masses.

Balmer ($H\beta$) BLR sizes and masses have been measured for about 40 AGNs, including five NLS1s (Wandel, Peterson, & Malkan 1999; Kaspi et al. 2000; Peterson et al. 2000; Shemmer et al. 2001). These results suggest that NLS1s have BLR sizes comparable to those of S1s with similar optical luminosities. Moreover, NLS1 and S1 galaxies delineate a broad mass-luminosity relationship with the former sources populating the low mass extremum of this relationship. This is consistent with the hypothesis that NLS1s are undermassive black hole systems with higher accretion rates and/or sources viewed nearly face-on.

To distinguish between various models requires systematic measurements of the black hole masses M , mass accretion rates \dot{M} , broad-line region sizes R_{BLR} , and source inclinations i of NLS1s and other S1s. These key parameters may all be measured directly or inferred through application of echo mapping (reverberation) techniques (Blandford & McKee 1982; Peterson 2001) that use the relative responses of continuum and emission-line components to constrain strongly the nature of the responding emission regions. The responsivity-weighted BLR size is given approximately by $R_{\text{BLR}} = \tau c$, with τ the time lag, measured from cross-correlation analysis, between the continuum and delayed, radiatively driven emission-line variations. Combining R_{BLR} with the emission-line velocity full-width-half-maximum V_{FWHM} , assumed to be gravitationally determined and derived from the variable line profile, virial masses M follow from $M = f V_{\text{FWHM}}^2 R_{\text{BLR}} / G$, with f a factor of order unity that depends on the detailed emission-line gas distribution (and which may be determined by measuring the velocity-dependent emission-line response). The results of Wandel et al. (1999), Kaspi et al. (2000), and Peterson et al. (2000) are based on these reverberation techniques. The magnitude and wavelength-dependence of any continuum time delays, when combined with the spectral energy distribution, may be used to constrain the product $M\dot{M}$ under certain conditions (Collier et al. 1999), hence \dot{M} follows given M from the associated emission-line reverberation measurement. The width of the continuum delay distribution at many wavelengths and the velocity dependent emission-line response (e.g., Welsh & Horne 1991) may be used to measure the source inclination. These methods for measuring \dot{M} and i have not been applied with much success to existing datasets, since they lack sufficient signal-to-noise and monitoring duration. Other methods for measuring i include accretion disk fitting to Fe K α (e.g., Nandra et al. 1997) and combined UV continuum and $H\beta$ measurements (Rokaki & Boisson 1999).

We undertook a program of coordinated multiwavelength observations of the NLS1 galaxy Akn 564 ($z = 0.0247$, Huchra, Vogeley, & Geller 1999) in the summer of 2000. Akn 564 is the brightest known NLS1 galaxy in the 2–10 keV band, with hard X-ray luminosity $L_X \simeq 10^{43.4} \text{ erg s}^{-1}$ (Turner et al. 2001). It has a steep power-law continuum ($\Gamma_{\text{hard}} \approx 2.5$), ionized Fe K line features, and a steep soft excess, as described by Turner et al. (2001). A 35 day *ASCA* observation shows evidence for flux variations of $\approx 36\%$ (Turner et al. 2001, Edelson et al. 2001). Optical monitoring

by Giannuzzo et al. (1998) reveals $H\beta$ variations of about 8% on time scales of about 4 years, rather lower than observed in other S1 galaxies over similar periods (e.g., about 25% for NGC 5548). Optical spectra reveal the presence of strong [Ca II] and Fe II emission (van Groningen 1993). No program of UV monitoring has been previously undertaken on this source, but §3 presents an archival IUE observation. Our program included *ASCA* (Turner et al. 2001 hereafter, Paper I), *HST* (this paper), optical (Shemmer et al. 2001 hereafter, Paper III), and *RXTE* (Pounds et al. 2001) observations, and represents the most comprehensive contemporaneous multiwavelength study of a NLS1 galaxy to date. In this paper, we present the UV continuum and emission-line variability results obtained with *HST* during the period 2000 May 9 to July 8. These observations were primarily intended to measure the effective size of the UV BLR of a NLS1, and permit measurement of a virial mass M based on multiple emission lines, and thereby further constrain the nature of NLS1 galaxies. Akn 564 also has a rich UV absorption spectrum (Crenshaw et al. 1999), and discussion of our absorption-line results will be deferred to a later paper. In §2, we describe the observations. We discuss the properties of the mean spectra in §3. The continuum and emission-line variability are presented in §4 and §5, respectively. Our results are discussed and summarized in §6 and §7, respectively.

2. Observations

We observed the nucleus of Akn 564 with the Space Telescope Imaging Spectrograph (STIS) on the *Hubble Space Telescope* (*HST*) on 46 occasions during the period 2000 May 9 to July 8. The first five visits were separated by intervals of ~ 5 days. Beginning on the fifth visit (2000 May 29), the sampling interval was decreased to ~ 1 day for the remaining monitoring period. We obtained low-resolution spectra during each visit with the G140L and G230L gratings, thereby providing full UV coverage at a spectral resolution of approximately 1.2 \AA over the range 1150 – 1730 \AA and 3.2 \AA over the range 1570 – 3150 \AA . We used the $52'' \times 0''.5$ slit for the low-resolution spectra to maximize throughput and ensure accurate absolute photometry. As Akn 564 is a point source in the STIS spectral images, there was no significant resolution degradation by using the wide slit. The exposure times were 1200 and 520 seconds for each G140L and G230L spectrum, respectively, except on 2000 May 29, when the respective exposure times were 1434 and 816 seconds. To estimate the effects of the intrinsic absorption on the UV emission-line profiles, we obtained high-resolution echelle spectra of the nucleus on 2000 May 29 with the E140M grating at a spectral resolving power of $\lambda/\Delta\lambda \approx 45,000$. The E140M spectra were obtained through the $0''.2 \times 0''.2$ aperture during four consecutive orbits to yield a combined exposure time of 10,310 sec. The spectra were reduced using the IDL software developed at NASA’s Goddard Space Flight Center for the STIS Instrument Definition Team (Lindler 1998). For the low-dispersion spectra, we used standard point-source processing with an extraction height (perpendicular to the dispersion) of $0''.275$ to obtain flux-calibrated G140L and G230L spectra as a function of wavelength.

Small wavelength calibration uncertainties exist between spectra of a given grating. To

remove these effects, relative wavelength calibration of spectra for each grating is required. The methodology we employ is analogous to that described by Korista et al. (1995) (except we do not subtract a continuum fit from each spectrum). We cross-correlate the spectra near the emission-line peaks of Ly α λ 1216, C IV λ 1549, and He II λ 1640 for the G140L grating, and near the peaks of C III] λ 1909 and Mg II λ 2798 for the G230L grating. Hence, we determine the nearest whole pixel shifts for each spectrum relative to its appropriate mean spectrum. The majority of the spectra (about 90%) required either a one or zero-pixel shift, and the remaining spectra required a two-pixel shift. The uncertainty in our relative wavelength calibration is of order ± 0.5 pixels, i.e., about 0.6 Å and 1.7 Å for the G140L and G230L gratings, respectively. We made no attempt to intercalibrate the G140L and G230L spectra, given their difference in resolution.

3. Mean Spectra

The observed mean and root mean square (rms) of the 46 G140L and G230L spectra are presented in Figures 1 and 2, respectively. The rms spectra have been corrected for the bias due to measurement errors. Furthermore, these spectra have been corrected for Galactic reddening using $E(B - V) = 0.06$ mag. (Schlegel et al. 1998). We note narrow line Balmer decrement and He II λ 1640/He II λ 4686 ratios suggest internal reddening is potentially large for Akn 564 (Walter & Fink 1993; Paper III), i.e., $E(B - V) \approx 0.2$ mag. Determination of the internal reddening in Akn 564 will be discussed in a forthcoming paper, Crenshaw et al. 2001. The mean spectra are rich in both emission and absorption features. The prominent emission features have been identified and labelled in Figs. 1 and 2. Many of the unlabelled, poorer contrast features may be associated with Fe II emission. Intrinsic UV absorption in Ly α λ 1216, N V λ 1240, Si IV λ 1397, and C IV λ 1549 is present, along with Galactic absorption in lines such as Si IV λ 1397 and Mg II λ 2798 (Crenshaw et al. 1999). We have made no attempt to identify the complex of absorption features shortward of Ly α λ 1216, since this spectral region is affected by time-dependent residuals due to imperfect subtraction of geocoronal Ly α emission. We defer discussion of the rms spectra to §5.

In order to quantify the prominent emission-line characteristics, we determine pure emission-line spectra from which appropriate mean spectral measurements are then made. This was done through cubic spline interpolations over the absorption features and subtraction of a power-law fit to the continuum. Our spectral measurements (to be discussed in this section) assume zero internal reddening. The continuum is defined by four nominally line-free bands chosen by visual inspection of the mean spectrum, Fig. 1; 1155–1180 Å, 1350–1380 Å, 1460–1500 Å, and 1620–1660 Å. These bands only approximate the true continuum level, since Balmer recombination continuum, Fe II blends and other weak broad emission contaminate them to some extent. The rms spectrum, Fig. 1, indicates these bands are not notably biased by line variability. The best-fit continuum is described by $F_\lambda = k(\lambda/1000 \text{ Å})^\alpha$ with $\alpha = -0.88 \pm 0.01$ and $k = (1.56 \pm 0.01) \times 10^{-14} \text{ ergs s}^{-1} \text{ cm}^{-2} \text{ Å}^{-1}$. The continuum fit uncertainties are purely statistical and should be treated with caution, since systematic errors due to reddening, for example, are non-negligible. This UV continuum is redder

than $F_\lambda \propto \lambda^{-1.34}$, typically observed in quasars (O'Brien et al. 1988). This may be due to, for example, disk irradiation (assuming the UV emission arises in an accretion disk) and/or internal reddening. We choose to extrapolate this continuum into the G230L spectral range, since here the continuum level is poorly defined, as the aforementioned contaminants strengthen. We note, in this regime, the extrapolated continuum is about 30% below the local, pseudo-continuum defined largely by the Fe II blends. The validity of the above continuum fit awaits detailed consideration of these Fe II blends and corrections for internal reddening.

Our emission-line spectral measurements are detailed in Table 1. For each emission line in column (1) we give the FWHM ($FW_{0.5}$) in column (2) and flux contained therein ($F_{0.5}$) in column (3). Similarly, columns (4) and (5) give the full width at 20% maximum intensity ($FW_{0.2}$), and flux therein ($F_{0.2}$). Column (6) gives the line centroid $\lambda_{0.2}^{cen}$, defined by $F_{0.2}$. No attempt has been made to deconvolve blended lines, hence column (1) refers to the primary emission line only. In Table 1, columns (4) through (6) are empty for $C\text{III}]\lambda 1909$ and $Mg\text{II}\lambda 2798$ because $F_{0.2}$ is ill-defined, $C\text{III}]\lambda 1909$ is blended with $Si\text{III}]\lambda 1892$ and the estimated, extrapolated continuum near $Mg\text{II}\lambda 2798$ is significantly below the observed level. We note that all values in Table 1 are in the observed frame. We chose to measure line fluxes at 20% maximum intensity to minimize the effects of line blending, by measuring the primary emission line flux only.

The uncertainties in the full width and flux measurements (Table 1) are dominated by systematic errors attributable to uncertainties in the applied absorption (where applicable) and reddening corrections. We assess the uncertainty associated with our absorption corrections by using cubic spline and linear interpolations over the $Ly\alpha\lambda 1216$ absorption feature. Figure 3 presents an illustrative example of the ambiguity in the $Ly\alpha\lambda 1216$ emission line profile due to the different interpolation schemes. We find uncertainties of $\sim 15\%$ and 8% for our line width and flux measurements, respectively. We do not consider the systematic uncertainty in our applied reddening corrections, given the aforementioned possibility of large internal reddening. For wavelengths $\gtrsim 1800\text{\AA}$, systematic errors of $\sim 30\%$ due to uncertainties in our continuum fit may be important, but are not considered further.

The $Ly\alpha\lambda 1216$, $N\text{V}\lambda 1240$, and $C\text{IV}\lambda 1549$ emission lines have FWHMs of $\approx 2000\text{ km s}^{-1}$, compared to typical values of $\sim 5000\text{ km s}^{-1}$ for S1 galaxies. Their $FW_{0.2}$ values are $\approx 4000\text{ km s}^{-1}$. For $He\text{II}\lambda 1640$, the $FW_{0.5}$ and $FW_{0.2}$ estimates are ≈ 1000 and 3000 km s^{-1} , respectively (from the mean G140L spectrum).

The emission-line profiles appear symmetric about their systemic wavelengths, but this is difficult to quantify due to contaminating emission, such as $[O\text{III}]\lambda 1664$ in the red wing of $He\text{II}\lambda 1640$, and absorption features affecting many of the line profiles. The centroids, $\lambda_{0.2}^{cen}$, of the observed emission-line fluxes of $Ly\alpha\lambda 1216$, $N\text{V}\lambda 1240$, $Si\text{IV}+O\text{IV}]\lambda 1400$, $C\text{IV}\lambda 1549$, $N\text{III}]\lambda 1750$, and $Mg\text{II}\lambda 2798$ are consistent with those expected based on the systemic redshift $z = 0.0247$, given the 1.2\AA and 3.2\AA spectral resolutions of the G140L and G230L gratings. The $[O\text{I}]\lambda 1336$ and $N\text{IV}]\lambda 1523$ emission-line flux centroids are redshifted and blueshifted by 2.5\AA and 1.6\AA ,

respectively. The $[\text{O I}] \lambda 1336 \lambda_{0.2}^{\text{cen}}$ is possibly biased by $\text{S II} \lambda 1340$ emission. The $\text{He II} \lambda 1640$ emission-line flux centroid is blueshifted by 1.3\AA ($\approx 230 \text{ km s}^{-1}$). The $\text{He II} \lambda 1640 \lambda_{0.2}^{\text{cen}}$ measured from the G230L mean spectrum is most likely biased by $[\text{O III}] \lambda 1664$ contamination. Figure 4 presents the mean $\text{Ly}\alpha \lambda 1216$, $\text{C IV} \lambda 1549$, and $\text{Mg II} \lambda 2798$ emission line profiles as a function of velocity, with the above defined continuum fit subtracted. The emission line profile amplitudes have been normalized to unity. The high ionization lines of $\text{Ly}\alpha \lambda 1216$ and $\text{C IV} \lambda 1549$ and the low ionization line of $\text{Mg II} \lambda 2798$ do not appear notably blueshifted or redshifted relative to systemic velocities. These results are discussed in §6.1.

We find some significant differences between emission-line flux ratios in Akn 564 relative to those of more typical Seyfert 1 galaxies. From Table 1, measured line ratios for Akn 564 are $(\text{C IV}/\text{Ly}\alpha) = 0.27(1.09)$, $(\text{C III}]/\text{Ly}\alpha)^* = 0.16(0.13)$, $(\text{C III}]/\text{C IV})^* = 0.65(0.12)$, $(\text{Si IV} + \text{O IV}]/\text{C IV}) = 0.48(0.07)$, $(\text{Si IV} + \text{O IV}]/\text{Ly}\alpha) = 0.13(0.08)$, $(\text{Mg II}/\text{Ly}\alpha)^* = 0.33(0.22)$, and $(\text{He II}/\text{C IV}) = 0.78(0.09)$. The line ratios in parenthesis are those for the S1 galaxy NGC 5548, taken from Clavel et al. (1991). Line ratios with an asterisk denote those (for Akn 564) estimated using the fluxes at 50% maximum intensity, compared to 20% for the others. This was necessary because, as mentioned previously, $F_{0.2}$ is ill-defined for $\text{C III}]\lambda 1909$ and $\text{Mg II} \lambda 2798$. The uncertainties in these line ratios are dominated by systematic effects, discussed above, and are of order 25%. This error estimate includes an $\sim 15\%$ bias due to excluding flux in the line-wings. For line ratios that include $\text{C III}]\lambda 1909$ and $\text{Mg II} \lambda 2798$, the error estimate may be notably underestimated on account of the continuum fit uncertainties described above. Our emission-line ratios show Akn 564 exhibits weaker $\text{C IV} \lambda 1549$ and stronger $\text{Si IV} + \text{O IV}]\lambda 1400$ emission compared to NGC 5548. These results are consistent with earlier results of Wilkes et al. (1999) and Kuraszkiewicz et al. (2000). We note our $\text{Mg II}/\text{Ly}\alpha$ ratio of 0.33 is notably larger than the mean value of 0.05 derived from the small sample of NLS1s by Kuraszkiewicz et al. (2000). This is probably largely attributable to different continuum level estimates near to $\text{Mg II} \lambda 2798$.

Finally, we checked archival IUE observations of Akn 564 to assess whether it was in a comparatively low or high flux state. Figure 5 presents the IUE SWP observation of 1984 Jan 17. For comparison purposes, our mean G140L spectrum of Fig. 1 is overlaid as the thicker line. Both spectra have been corrected for Galactic reddening as detailed above. The continuum and emission-line fluxes are in qualitative agreement. In particular, the $\text{Ly}\alpha \lambda 1216$ and $\text{N V} \lambda 1240$ line profiles are very similar; and suggest negligible emission-line flux differences between the 1984 and 2000 observations. Other IUE observations from 1981 are also in qualitative agreement with our observations.

4. Continuum Variability Characteristics

4.1. Light Curves

We select five nominal continuum bands by visual inspection of the mean and rms spectra presented in Figs. 1 and 2: 1350–1380Å, 1460–1500Å, 1620–1660Å, 2070–2130Å, and 2960–3040Å, henceforth referred to by their mean observed wavelengths 1365Å, 1480Å, 1640Å, 2100Å, and 3000Å, respectively. We re-iterate that each of these continuum bands overestimates the true continuum level on account of various contaminants (§3). These bands are not notably biased by emission-line variability, and thereby provide good approximations for the continuum variability at these wavelengths. Light curves, describing the continuum variability during the 60-day monitoring period, are presented in Figure 6, with the continuum bands as labelled. We note our observed continuum flux measurements are not corrected for reddening.

All the continuum regions show the same qualitative behavior. The 1365Å variations may be described by; an increase in flux of $\sim 20\%$ during the first 15 days, followed by a decrease of $\sim 16\%$ over the next 5 days. These variations are followed by two flares at about $\text{JD} - 2450000 \approx 1697$ and 1711. The rising trough-to-peak variations are about 18% in ~ 3 days, with similar declining peak-to-trough variations occurring over longer time scales of several days. Both flare events appear to be asymmetric, the later one more so and of longer duration. Between these two events was a relatively quiescent period of about 5 days. Thereafter, the variations are less pronounced, at about the 5% level. For the longer wavelength variations, at 2100Å and 3000Å, the rms variations are of reduced amplitude with broader asymmetric flare profiles. The peaks of the 3000Å flares are delayed, relative to those at 1365Å, by 1-2 days. The contemporaneous ASCA observations exhibit larger amplitude correlated variations (including similar but narrower twin flare events), possibly delayed by about 0.4 days (Papers I and III). We note the continuum variations may be slightly undersampled during the intensive monitoring period of $\text{JD} - 2450000 \approx 1694$ –1734, and are definitely undersampled for prior times, given that $\sim 10\%$ flux amplitude changes on time scales of 1 day are evident (see below).

We characterize the 1365–3000 Å variations by measuring two common variability parameters: the ratio of the maximum to minimum flux R_{\max} and the amplitude of the intrinsic variability relative to the mean flux F_{var} . The latter is corrected for the measurement errors ε ,

$$F_{\text{var}} = \frac{1}{\bar{F}} \sqrt{(\sigma_F^2 - \Delta^2)}, \quad (1)$$

where \bar{F} , σ_F , and $\Delta^2 = (1/N) \sum_{i=1}^N \varepsilon_i^2$ are respectively the standard mean flux, rms flux, and mean square of the measurement errors, with $N = 46$ the number of data points in the light curve (Edelson, Krolik, & Pike 1990, Rodríguez-Pascual et al. 1997b). The results are presented in Table 2 for each of the light curves, as listed in column (1). Columns (2)–(5) give, respectively, the mean flux \bar{F} , the rms flux σ_F , F_{var} , and R_{\max} . Both F_{var} and R_{\max} are potentially biased by constant flux components, e.g., Fe II emission. However, these effects are likely to be small. On time scales of about 60 days, the fractional amplitude of the intrinsic variations is essentially constant between 1365 Å and 2100 Å at about 6%, with the full range of variations $R_{\max} - 1 \approx 0.31$. At 3000Å the

fractional variability amplitude is about 4%, with the full range of variations $R_{\max} - 1 \approx 0.19$. This level of intrinsic UV variability is about a factor 3 less than that found in typical S1 galaxies, which typically display fractional flux variations $F_{\text{var}} \approx 18\%$ on time scales of 60 days (Collier, Peterson & Horne 2001).

The 1365–1640 Å continuum variations show evidence for $\sim 10\%$ flux amplitude changes on time scales of about 1 day, as seen in the events beginning at about JD – 2450000 ≈ 1696 , 1710, and 1707, and suggest a fraction of the UV continuum emitting region must come from a compact region of $\lesssim 1$ light day in size. The 2100–3000 Å variations show evidence for reduced flux amplitude changes of $\sim 5\%$ on similar time scales. For comparison, in S1 galaxies far UV variations of about 5% rms occur on similar time scales (e.g., Korista et al. 1995; Welsh et al. 1998). These faster, larger amplitude variations suggest NLS1s (at least Akn 564) exhibit more variability power on short (day) time scales. We confirm this through an autocorrelation analysis. Figure 7 presents the Akn 564 1365Å (solid line) and NGC 7469 (a S1 galaxy) 1315Å (dotted line) autocorrelation functions (ACFs). The relative steepness of the 1365Å ACF (compared to the 1315Å ACF) indicates Akn 564’s fluctuation power density spectrum is flatter than that for NGC 7469, and thereby exhibits more power on short time scales. We note Pounds et al. (2001) have shown that the X-ray variations in Akn 564 are faster than those of typical S1 galaxies. The full-width-half-maximum of the ACFs are 3.27 and 4.93 days for Akn 564 and NGC 7469, respectively, and are indicative of characteristic UV variability time scales. By assuming the mass ratio of the sources is determined by the variability time scale ratio of 0.66, we estimate the mass of Akn 564 to be $M \sim 5 \times 10^6 M_{\odot}$, given a mass estimate for NGC 7469 of $8 \times 10^6 M_{\odot}$ (Wandel et al. 1999). This mass estimate (for Akn 564) is in good agreement with that derived from our emission-line reverberation results, discussed in §6.2.

4.2. Cross-Correlation Analysis

The continuum light curves of Fig. 6 clearly display correlated variations between 1365–3000 Å. The peaks and troughs of the flare events at JD – 2450000 ≈ 1697 and 1711 occur approximately simultaneously; as mentioned above, the 3000Å flare peaks appear delayed by about 1-2 days relative to those at shorter wavelengths. Differences between the light curves are also evident, for example, decay time scales for the two flares appear comparatively longer at wavelengths $\geq 2100\text{\AA}$, and short (day) time scale 1365Å variations appear washed out at 3000Å. In order to quantify the nature of the correlations between continuum variations we undertook a cross-correlation analysis. Two algorithms were employed to compute cross-correlation functions (CCFs), the interpolated CCF (ICCF) of Gaskell & Sparke (1986) as implemented by White & Peterson (1994), and the Z -transformed discrete correlation function (ZDCF) algorithm of Alexander (1997). For our data, the results recovered by the two algorithms are in agreement.

Figure 8 shows the CCFs obtained by cross-correlating each of the four longer-wavelength continuum light curves with the 1365 Å light curve. The solid line and data points with error

bars show the ICCF and ZDCF CCFs, respectively, and are in good agreement. The 1365–3000 Å variations are highly correlated as evidenced by maximum values of the cross-correlation coefficients $r_{\max} \approx 0.9$. The 1480–2100Å CCFs all peak at about zero lag, thereby suggesting these continuum variations occur quasi-simultaneously. The 3000Å CCF peaks away from zero at about 0.5 days. The 2100Å and 3000Å CCFs appear asymmetric, compared to the 1480Å and 1640Å CCFs, and suggest their responses extend over a larger range of positive delays. Figure 9 presents similar CCFs for four optical continuum regions; 4875–4915Å, 5197–5237Å, 6551–6622Å, and 6935–7004Å, henceforth referred to by the observed wavelengths 4900Å, 5200Å, 6600Å, and 6900Å, respectively (for consistency with Paper III). The optical data are from Paper III. These CCFs have been computed as described above. The optical variations are correlated with those at UV wavelengths with $r_{\max} \approx 0.5$. The decreasing maximum correlation coefficient with optical wavelength is likely due to progressively less coherent time delay smeared responses and/or increasing noise dilution (see Table 4 in Paper III). The optical CCFs clearly peak away from zero at about 2 days.

Table 3 summarizes our cross-correlation results. Column (1) lists the light curve that has been cross-correlated with the 1365 Å continuum light curve. Columns (2) and (3) give the centroid of the CCF τ_{cen} , as determined by the ICCF and ZDCF algorithms. The ICCF centroid is calculated over all points above 0.8 times the maximum cross-correlation coefficient r_{\max} , whereas the ZDCF centroid is computed from all points near the peak with a cross-correlation amplitude above half that of the peak. Columns 4 and 5 report the time delay τ_{peak} , measured from the peak of the CCF. Columns 6 and 7 give r_{\max} , for the ICCF and ZDCF, respectively. Column 8 details the FWHM of the ICCF. The reported errors on τ_{peak} and τ_{cen} for the ICCF are the $1-\sigma$ uncertainties as determined by the model-independent quasi-bootstrap and flux randomization method of Peterson et al. (1998). We find no evidence for lags between the 1365 Å and 1640 Å light curves, as evidenced by peak and centroid lag measurements consistent with zero. The 2100 Å and 3000Å variations, however, lag those at 1365 Å by ~ 0.3 and 1.0 day, respectively. Here and hereafter, we note the centroid lags since they are a less biased estimator of the size of the responding emission region. These lags are greater than zero at 94% and 99%, respectively. The optical variations at ~ 5000 Å lag behind those at 1365 Å by about 2 days at no less than 99% confidence. The optical variations at wavelengths longer than 6000 Å appear to lag those at 1365 Å by a similar amount, although statistically the suggested lags are not significantly different from zero on account of their very low amplitude ($\sim 1\%$) variability; which is comparable to the measurement errors.

We investigate these wavelength-dependent continuum lags further by binning the 46 G140L and G230L spectra (covering 1150–3140Å) into 40 Å bins, and forming light curves based on the total flux in each bin. We cross-correlate (using the ICCF) each of these light curves with the 1365 Å light curve. The results are presented in Figure 10. In the top panel, the histogram plot shows the centroid lag for each bin as a function of the bin wavelength, thus producing a “lag spectrum”. The corresponding values of r_{\max} are shown in the lower panel. Again, the error bars

for each bin in the upper panel were determined by the method of Peterson et al. (1998). The solid line represents the best-fit function $\tau \propto (\lambda^\gamma - \lambda_0^\gamma)$, with $\lambda_0 = 1365 \text{ \AA}$, $\gamma = 2.4 \pm 0.1$, and reduced chi-squared $\chi_\nu^2 = 0.07$ for $\nu = 50$ degrees of freedom, to the lag measurements. The small value of $\chi_\nu^2 << 1$ suggests the lag uncertainties may be overestimated. There is a clear trend of increasing lag with wavelength throughout the UV: the variations at 3100 \AA lag those at 1365 \AA by about 0.9 days. The lag measurements for $\lambda \gtrsim 2050 \text{ \AA}$ are non-zero at no less than 90% confidence. For wavelengths shorter than 2050 \AA , the lag measurements are consistent with zero delay. The 1150 – 3140 \AA variations are well correlated with $r_{\max} \approx 0.9$. In the region where the G140L and G230L spectra overlap, i.e., ~ 1600 – 1700 \AA , the lag measurements are in good agreement. The lag spectrum is reasonably smooth with no clear positive deviations near the emission-line wavelengths, as would be the case if the emission-line response time scales were measurably larger. Similarly, there are no negative dips in the maximum correlation coefficient spectrum, with the possible exception near Mg II $\lambda 2798$. These results support the negligible presence of emission-line variability to be discussed in §5. We note the dip in the maximum correlation coefficient at about 1700 \AA is due to calibration uncertainties in the G230L spectra. Similarly, the slight depression in r at $\lesssim 1200 \text{ \AA}$ is due to calibration errors in the G140L spectra. We note the two bins with the largest centroid lag errors are those contaminated by Ly α $\lambda 1216$ and Mg II $\lambda 2798$.

We use the optical lag measurements (Table 3) to extend the UV lag spectrum. The UV/optical lag spectrum is presented in Figure 11. The solid line represents the best-fit function $\tau \propto (\lambda^\gamma - \lambda_0^\gamma)$, with $\lambda_0 = 1365 \text{ \AA}$, $\gamma = 1.3 \pm 0.1$, and $\chi_\nu^2 = 0.09$ for $\nu = 54$ degrees of freedom. The dotted line represents the best-fit function to the UV data alone (as in Fig. 10), i.e., with $\gamma = 2.4 \pm 0.1$. By including the optical data, the lag–wavelength relationship appears to flatten.

5. Emission-Line Variability

The largely featureless rms spectra of Figs. 1 and 2 immediately show that any emission-line variability is of low amplitude. Figure 1 shows Ly α $\lambda 1216$, N V $\lambda 1240$, Si IV+O IV] $\lambda 1400$, C IV $\lambda 1549$, and He II $\lambda 1640$ variations are present with amplitudes of < 4 , 5 , 6 , 5 , and 4% , respectively. Figure 2 indicates Si III $\lambda 1892$, C III] $\lambda 1909$, and Mg II $\lambda 2798$ variations with amplitudes of < 6 , 6 , and 4% , respectively. For cases where emission-line variations are present or suggested, the bulk of the variation occurs in the core of the line. The variations at these wavelengths, for emission lines contaminated by intrinsic absorption, may be a superposition of both emission and absorption-line variability. A discussion of the latter is deferred to a later paper. We note the N V $\lambda 1240$ variations appears to be slightly asymmetric, with a deficit of response in its blue wing. The variations at about 1215 \AA are spurious, and attributable to time-dependent residuals from imperfect subtraction of geocoronal Ly α emission.

Emission-line light curves were constructed by direct integration, summing the flux in specified, absorption-free wavelength regions after subtracting a continuum defined by a linear fit to the nearest continuum regions on either side of the emission-line region. Our attempts

at validating and possibly improving our direct integration light curves through spectral fitting with the IRAF task SPECFIT (Kriss 1994) failed. This was because the spectral complexity of the emission-line profiles permitted too much freedom in the fitting process such that artificial emission-line variations were introduced by corresponding changes in the adopted absorption profile. The blanket exclusion of any absorption regions from our variable emission-line flux regions, defined by their respective rms spectra (Figs. 1 and 2), severely inhibited our ability to extract the already low-amplitude variations. We were only able to extract significant emission-line variations for Ly α $\lambda 1216$. The comparatively smaller fluxes and larger measurement errors for the other emission-lines precluding extraction of significant variations.

Figure 12 presents the Ly α $\lambda 1216$ light curves for the monitoring period. The data points with error bars describe the emission-line variations between 1240–1243 Å and 1247–1250 Å (“light curve 1”), and the dashed line those between 1240–1250 Å (“light curve 2”); the latter includes any possible variable contribution from the intrinsic H I absorption feature. In both cases the continuum is defined by a linear fit between 1155–1180 Å and 1350–1380 Å. The 1365 Å light curve, §4.1, is scaled and vertically shifted to fit light curve 1, and is shown by the solid line. We note our observed emission-line flux measurements are not corrected for reddening.

The Ly α $\lambda 1216$ variations resemble those of the continuum, but with greatly reduced amplitude and appear delayed by about a few days. In each case, the flux increases by $\sim 3\%$ during the first 15 days, and similar flare events occur at similar times, i.e., $JD - 2450000 \approx 1697$ and 1711. The contrast of any features in the light curves is poor on account of the low-amplitude variability, which is comparable to the measurement uncertainties. On time scales of about 60 days, the intrinsic line variations are $\sim 1\%$, with the full range of variation $\sim 7\%$. Moreover, the Ly α $\lambda 1216$ light curves are clearly well correlated and exhibit similar variability patterns. These results suggest any intrinsic H I absorption-line variability does not notably affect the emission-line variations.

Cross-correlation of the Ly α $\lambda 1216$ and 1365 Å variations quantifies their apparent similarity. Our results are presented in Figure 13 and Table 3. Figure 13 presents Ly α $\lambda 1216$ CCFs for both line light curves detailed above. The solid line and filled data points represent the ICCF and ZDCF CCFs, respectively, as described earlier, for light curve 1, and the dashed line and open data points are for light curve 2. The Ly α $\lambda 1216$ variations are correlated with the 1365 Å variations with a maximum cross-correlation amplitude $r_{\max} \approx 0.5$. The probability of exceeding $r \approx 0.5$ in a random sample of observations (of the same number, $N = 45$, as here) drawn from an uncorrelated parent population is about 0.1% (Bevington & Robinson 1992), thereby the Ly α $\lambda 1216$ variations are correlated with those at 1365 Å at about 99.9% confidence. The formal significance of this correlation is most likely over-estimated, since not all correlated data points are independent. Detailed simulations will be required in order to quantify the magnitude of this bias. By directly cross-correlating light curves 1 and 2, we confirm they are correlated with essentially zero time delay. The peak and centroid lag measurements for light curves 1 and 2 are consistent to within the large uncertainties. Moreover, for light curve 1 the lag measurements are consistent with zero

delay. Our results only permit an upper limit for the size of the Ly α λ 1216 emission region, $R_{\text{BLR}}^{\text{Ly}\alpha}$ \lesssim 3 light days. We caution, the low amplitude Ly α λ 1216 variations may indicate the bulk of the emission region is at larger radii, as discussed in §6.2.

6. Discussion

6.1. Nature of the UV Broad Line Region

A complete study of the nature of the UV BLR of Akn 564 requires detailed photoionization modelling of the spectral energy distribution and is beyond the scope of this paper. Here, we offer a preliminary discussion of our results in the context of previous work.

The BLR of Akn 564 is characterised by smaller gas velocity dispersions (as determined by the emission-line velocity full-width-half-maximum) than found in typical S1 galaxies (§3), as noted earlier by Rodríguez-Pascual et al. (1997a), i.e., about 2000 km s^{-1} compared to 5000 km s^{-1} . These authors found evidence for similar magnitude UV line widths in about a dozen NLS1s; see also Kuraszkiewicz et al. (2000). The full widths of the low and high-ionization lines are comparable, see Fig. 4, and interestingly similar to those of the N III] λ 1750 and C III] λ 1909 intercombination lines. For example, the full widths of He II λ 1640, N III] λ 1750, C III] λ 1909, and Mg II λ 2798 are 1800, 1900, 1900, and 1700 km s^{-1} , respectively (Table 1; as measured from the G230L spectra).

As noted in §3, the broad emission-line profiles of Akn 564 are approximately symmetric about their systemic wavelengths. These results, and those above, contrast with UV/optical observations of quasars (e.g., Gaskell 1982; Wilkes 1984; Corbin 1991) and S1 galaxies, showing that high-ionization lines are shifted blueward of low-ionization lines, which are approximately at systemic redshifts, and slightly broader. Leighly (2000) presented observations of two NLS1s (IRAS 13224-3809 and 1H 0707-495) which also showed the high ionization lines were strongly blueshifted and much broader than the low ionization Mg II λ 2798 line, similar to results for the NLS1 galaxies 1 Zw 1 and NGC 4051 presented by Laor et al. (1997) and Peterson et al. (2000), respectively. Collinge et al. (2001) find the C IV λ 1549 line in NGC 4051 to be blueshifted by about 100 km s^{-1} . These prior results are often interpreted as evidence for BLR radial motions. The low ionization lines may arise in an accretion disk, with the high ionization lines emitted in a wind launched from this disk (e.g., Collin-Souffrin et al. 1988). Our results suggest an absence of outflowing high ionization BLR gas with velocities $\gtrsim 230 \text{ km s}^{-1}$ in Akn 564. Moreover, the approximate symmetry of the emission-line profiles may indicate the predominance of optically thin broad line emission, since it is emitted essentially isotropically and traces the full velocity field (Netzer 1976; Davidson 1977; Shields, Ferland, & Peterson 1995).

The level of intrinsic line variability is notably less than observed in typical Seyfert 1 galaxies over comparable time scales (§5). For example, NGC 5548 (Korista et al. 1995) showed Ly α λ 1216, C IV λ 1549, and He II λ 1640 variations of $\sim 13\%$, $\sim 9\%$, and $\sim 14\%$, respectively. Similarly,

the same lines in NGC 7469 (Wanders et al. 1997) showed variations of $\sim 10\%$, $\sim 9\%$, $\sim 14\%$. This difference may simply be a consequence of the reduced level of assumed ionizing continuum variations combined with geometrical dilution due to the finite BLR size. To investigate this scenario we convolved the observed continuum variations with thin shell broad line regions at radii of 6 and 2 light days (i.e., the predicted sizes of the Ly α $\lambda 1216$ and He II $\lambda 1640$ emission regions, see §6.2), respectively. In these cases, we find Ly α $\lambda 1216$ and He II $\lambda 1640$ variations of order 3 and 6%, respectively. These results suggest this type of scenario does not completely explain the reduced level of emission-line variability in Akn 564. On the other hand, the line-emitting gas in Akn 564 may be fully ionized in hydrogen, and hence optically thin to the Lyman continuum. This would lead to greatly reduced emission-line variability, with detectable variations occurring only for sufficiently large continuum variations that induce significant changes in the ionization structure of the emission region. Similarly, this scenario alone is likely insufficient to account for the lack of line variability across the observed range of ionization, as evidenced by the calculations of Ferland & Mushotzky (1982). However, we note these calculations are more appropriate for S1 BLRs, and thereby may be misrepresentative of NLS1s. Some combination of both the above effects appears a reasonable explanation for the reduced level of emission-line variability in Akn 564.

The unusual UV spectral properties of Akn 564 (§3), combined with stronger ionizing fluxes relative to other S1 galaxies, suggest NLS1s BLRs have a physically distinct nature from those found in S1 galaxies and quasars. Kuraszkiewicz et al. (2000) posit NLS1 BLRs characterized by gas cloud densities $n_H \approx 10^{11} \text{ cm}^{-3}$, ionization parameters $U \approx 0.01$, and BLR radii $R_{\text{BLR}}^{\text{UV}} \approx 20$ light days. On the other hand, Rodríguez-Pascual et al. (1997a) posit $n_H \approx 10^{7.5} \text{ cm}^{-3}$, $U \approx 0.3$, and BLR radii $R_{\text{BLR}}^{\text{UV}} \approx 2$ light days; under these conditions the broad line emitting gas becomes fully ionized in hydrogen, and thereby optically thin to the Lyman continuum. Our emission line profiles and variability results hint at a predominance of optically thin broad line emitting gas in Akn 564. In combination with a small estimated BLR size, §5, of $\lesssim 3$ light days, these conditions appear more readily reconcilable with those suggested by Rodríguez-Pascual et al. (1997a), as noted above.

6.2. Evidence for a Black-Hole Accretion Disk System

The wavelength-dependent continuum time delays of §4.2 suggest a stratified continuum reprocessing region extending a couple of light days from the central black hole, and provide possible evidence for an accretion-disk structure (Collier et al. 1998). Simple irradiated accretion disk models with radial temperature profiles $T \propto R^{-3/4}$ predict $\tau \propto \lambda^{4/3}$. Flatter temperature profiles predict steeper $\tau-\lambda$ relationships, and are realizable with, e.g., irradiated flared accretion-disk models. These models may be able to explain the steeper UV lag spectrum presented in §4.2. The fine details are determined by the geometry and structure of the accretion disk, relative prominence of viscous heat dissipation and irradiation effects, and the emission physics. Vaughan et al. (1999) present evidence, based on X-ray data, for a strongly ionised disk in Akn 564. Given

the close proximity of the UV and X-ray emitting regions (§4 and Papers I and III), our results support their conclusions. In the case of NGC 7469, the only other source with a clear detection of wavelength-dependent continuum lags (Wanders et al. 1997, Collier et al. 1998, Kriss et al. 2000), the UV/optical lag spectrum was consistent with $\tau \propto \lambda^{4/3}$, and is similar to that observed in §4.2. On the other hand, these continuum lags may be a result of diffuse continuum emission from broad-line emitting clouds (Korista & Goad 2000), or some combination of both these effects.

In §5 we estimated an upper limit of 3 light days for the size of the $\text{Ly}\alpha \lambda 1216$ broad line emitting region, $R_{\text{BLR}}^{\text{Ly}\alpha}$. We may compare this estimate with that expected on the basis of results obtained for other AGNs by using the Balmer emission region size $R_{\text{BLR}}^{\text{H}\beta}$ –luminosity relationships of Kaspi et al. (2000) and Peterson et al. (2000). The luminosity $\lambda L_{\lambda}(5100 \text{ \AA}) = \lambda F_{\lambda}(5100 \text{ \AA})4\pi D^2 \approx 2.4 \times 10^{43} \text{ erg s}^{-1}$, adopting a mean flux $F_{\lambda}(5100 \text{ \AA}) = 4 \times 10^{-15} \text{ erg s}^{-1} \text{ cm}^{-2} \text{ \AA}^{-1}$ and a distance $D = cz/H_0 = 99 \text{ Mpc}$ (assuming $H_0 = 75 \text{ km s}^{-1} \text{ Mpc}^{-1}$). This leads to an estimate for the size of the $\text{H}\beta$ -emitting region $R_{\text{BLR}}^{\text{H}\beta} \approx 12$ light days from the $R_{\text{BLR}}^{\text{H}\beta}$ –luminosity relationship shown in Fig. 6 of Peterson et al. (2000). From previous monitoring programs on S1 galaxies (Netzer & Peterson 1997), we can estimate the size of the $\text{Ly}\alpha \lambda 1216$ emitting region to be $R_{\text{BLR}}^{\text{Ly}\alpha} \approx 0.5R_{\text{BLR}}^{\text{H}\beta}$. Similarly, we expect that the highest ionization lines, $\text{N}\text{v} \lambda 1240$ and $\text{He II} \lambda 1640$, arise in a region of extent $\sim 0.2R_{\text{BLR}}^{\text{H}\beta}$. Based on the optical luminosity of Akn 564, we thus predict $R_{\text{BLR}}^{\text{Ly}\alpha} \approx 6$ light days and $R_{\text{BLR}}^{\text{N}\text{v}} \approx 2$ light days. The factor of ~ 2 difference between our measured and predicted values for $R_{\text{BLR}}^{\text{Ly}\alpha}$ is probably not significant, since the intrinsic scatter in the $R_{\text{BLR}}^{\text{H}\beta}$ –luminosity relationship is of order a factor 5. These results give us confidence our $R_{\text{BLR}}^{\text{Ly}\alpha}$ estimate is in the right ballpark.

By combining our $R_{\text{BLR}}^{\text{Ly}\alpha}$ upper limit of 3 light days with the emission-line velocity full-width-half-maximum $V_{\text{FWHM}} \approx 2500 \text{ km s}^{-1}$, derived from the rms emission-line profile (and assumed to be gravitationally determined), we estimate a virial mass upper limit from

$$M = f V_{\text{FWHM}}^2 R_{\text{BLR}}^{\text{Ly}\alpha} / G \lesssim 8 \times 10^6 M_{\odot}, \quad (2)$$

where for consistency with Wandel et al. (1999) and Kaspi et al. (2000) we use $f = 3/\sqrt{2}$. This mass estimate is consistent with the independent mass estimate of $M \sim 1 \times 10^7 M_{\odot}$ of Pounds et al. (2001), based on a fluctuation power spectrum analysis of X-ray variability in Akn 564. And is consistent with our mass estimate based on the variability arguments of §4.1. Furthermore, we note that the position of Akn 564 in the AGN mass–luminosity plane defined by Fig. 7 of Peterson et al. (2000), is consistent with the best-fit regression line based on the NLS1 galaxies alone, see Figure 14. This is consistent with the hypothesis that Akn 564 harbors a comparatively small black hole accreting with a higher accretion rate and/or is viewed more face-on than typical S1 galaxies; as found earlier by Pounds et al. (2001).

We conclude with a cautionary note concerning our derived upper limits for the size of Akn 564’s $\text{Ly}\alpha \lambda 1216$ BLR and black hole mass. The reduced continuum to $\text{Ly}\alpha \lambda 1216$ variations ratio of ~ 4 , relative to ~ 1 for the S1 galaxies NGC 5548 and NGC 7469 (references as given in §6.1), suggests our $\text{Ly}\alpha \lambda 1216$ reverberations arise from a region only about 1/4 of the size of the

$\text{Ly}\alpha \lambda 1216$ region probed by reverberation in S1 galaxies; and is therefore biased low. To illustrate the potential importance of this bias, assume that the $\text{Ly}\alpha \lambda 1216$ BLR is a thin shell of radius R . Equal time delay intervals define equal areas on the shell, and if our $\text{Ly}\alpha \lambda 1216$ response from < 3 light days is from only 1/4 of the area of the shell, we underestimate R by a factor of 4. This would lead to an $R_{\text{BLR}}^{\text{Ly}\alpha}$ upper limit of 12 light days. The bias in our black hole mass upper limit depends on the unknown nature of the gas velocity field, and is not readily quantifiable without better data.

7. Summary

An intensive two-month monitoring program on the NLS1 galaxy Akn 564 was undertaken with *HST* during 2000 May 9 to July 8. We summarize our results as follows.

1. The fractional variability amplitude of the UV continuum variations between 1365–3000 Å is about 6% on time scales of 60 days. This level of variability is about a factor of three less than that found in S1 galaxies. We find evidence for fast, large amplitude continuum variations, e.g., trough-to-peak flux changes of $\sim 18\%$ in about 3 days, atypical of those found in S1 galaxies that display similar amplitude variations on longer time scales.
2. We present evidence for wavelength-dependent continuum time delays. The continuum variations at 3000 Å lag behind those at 1365 Å by about 1 day. By combining the UV data with the optical data described in Paper III, we find that the variations at 5200 Å lag behind those at 1365 Å by about 2 days. These delays may be interpreted as evidence for a stratified continuum reprocessing region, possibly an accretion-disk structure. However, the delays may be a result of diffuse continuum emission from broad-line emitting clouds, or some combination of both these effects.
3. The $\text{Ly}\alpha \lambda 1216$ emission line exhibits intrinsic rms variations of about 1% on time scales of 60 days. These variations lag those at 1365 Å by $\lesssim 3$ days, and combining this with the line width yields a putative black hole mass limit of $\lesssim 8 \times 10^6 M_\odot$. This calculation assumes the line width is determined by the gravity of the black hole. We caution, the low amplitude $\text{Ly}\alpha \lambda 1216$ variations may indicate the bulk of the emission region is at larger radii, and thereby the veracity of our black hole mass limit is questionable. The possible bias in our black hole mass estimate is uncertain given the unknown nature of the gas velocity field. Despite the unreliability of our mass estimate, it is consistent with the independent estimate $M \sim 1 \times 10^7 M_\odot$ of Pounds et al. (2001), based on a fluctuation power spectrum analysis of X-ray variability in Akn 564.
4. The root-mean-square spectra suggest other strong emission line variability, e.g., of $\text{C IV} \lambda 1549$ and $\text{He II} \lambda 1640$, occurs with rms amplitudes of $< 5\%$. The low level of NLS1

emission-line variability is in contrast to that found in typical S1 galaxies, which display rms flux variations of $\sim 10\%$ on similar time scales.

We are pleased to acknowledge support for this work by NASA through grant number HST-GO-08265.01-A from the Space Telescope Science Institute, which is operated by the Association of Universities for Research in Astronomy, Inc., under NASA contract NAS5-26555. This research has made use of the NASA/IPAC Extragalactic Database (NED) which is operated by the Jet Propulsion Laboratory, California Institute of Technology, under contract with the National Aeronautics and Space Administration. SM acknowledges NASA grant NAG5-8913 (LTSA). We are grateful to an anonymous referee for useful comments.

REFERENCES

- Alexander, T. 1997, in *Astronomical Time Series*, ed. D. Maoz, A. Sternberg, & E.M. Leibowitz (Dordrecht: Kluwer), p. 163
- Baldwin, J., Ferland, G., Korista, K., & Verner, D. 1995, *ApJ*, 455, 119
- Bevington, P., & Robinson 1992, in *Data Reduction and Error Analysis for the Physical Sciences* (McGraw-Hill), p. 256
- Blandford, R., & McKee, C.F. 1982, *ApJ*, 255, 419
- Brandt, W. N., Fabian, A. C., Nandra, K., Reynolds, C. S., & Brinkmann, W. 1994, *MNRAS*, 271, 958
- Brandt, W. N., Mathur, S., Elvis, M. 1997, *MNRAS*, 285, 25
- Boller, T., Brandt, W. N., & Fink, H. 1996, *A&A*, 305, 53
- Boroson, T.A., & Green, R.F. 1992, *ApJS*, 80, 109
- Collier, S. et al. 1998, *ApJ*, 500, 162
- Collier, S., Horne, K., Wanders, I., Peterson, B.M. 1999, *MNRAS*, 302, 24
- Collier, S., Peterson, B. M., & Horne, K. 2001, in *Probing the Physics of AGN by Multiwavelength Monitoring*, ed. Peterson, B. M., Polidan, R. S., & Pogge, R. W., ASP v224, 457
- Collin-Souffrin, S., Dyson, J., McDowell, J., & Perry, J. 1988, *MNRAS*, 232, 539
- Corbin, M., *ApJ*, 1991, 371, 51
- Crenshaw, M., Kraemer, S., Boggess, A., Maran, S., Mushotzky, R., & Wu, C. 1999, *ApJ*, 516, 750
- Crenshaw, M. et al. 2001, in preparation
- Davidson, K. 1977, *ApJ*, 218, 20
- Edelson, R., Krolik, J., & Pike, G. 1990, *ApJ*, 359, 86.
- Edelson, R. et al. 2001, in preparation
- Ferland, G., & Mushotzky, R. F. 1982, *ApJ*, 262, 564
- Gaskell, C. M. 1982, *ApJ*, 263, 79
- Gaskell, C. M., & Sparke, L. 1986, *ApJ*, 305, 175
- Giannuzzo, M. E., Mignoli, M., Stirpe, G., & Comastri, A. 1998, *A&A*, 330, 894
- Goodrich, R. W. 1989, *ApJ*, 342, 224
- Guilbert, P. W., Fabian, A. C., & McCray, R. 1983, *ApJ*, 266, 466
- Huchra, J. P., Vogeley, M. S., Geller, M. J. 1999, *ApJS*, 121, 287
- Kaspi, S., Smith, P. S., Netzer, H., Maoz, D., Jannuzzi, B. T., & Giveon, U. 2000, *ApJ*, 533, 631
- Korista, K. et al. 1995, *ApJS*, 97, 285

- Korista, K. & Goad, M. 2000, ApJ, 536, 284
- Kriss, G. 1994, PASP Conference Series, v61, 437
- Kriss, G., Peterson, B. M., Crenshaw, D. M., & Zheng, W. 2000, ApJ, 535, 58
- Kuraszkiewicz, J., Wilkes, B., Czerny, B., & Mathur, S. 2000, ApJ, 542, 692
- Laor, A., Fiore, F., Elvis, M., Wilkes, B., & McDowell, J. C. 1997, ApJ, 477, 93
- Leighly, K. M. 1999a, ApJS, 125, 297
- Leighly, K. M. 1999b, ApJS, 125, 317
- Leighly, K. M. 2000, NewAR, 44, 395
- Lindler, D. 1998, CALSTIS Reference Guide (CALSTIS Version 5.1)
- Madau, P. 1988, ApJ, 327, 116
- Mathur, S., Elvis, M., & Wilkes, B. 1995, ApJ, 452, 230
- Nandra, K., George, I. M., Mushotzky, R. F., Turner, T. J., & Yaqoob, T. 1997, ApJ, 477, 602
- Netzer, H. 1976, MNRAS, 177, 473
- Netzer, H., & Peterson, B.M. 1997 in *Astronomical Time Series*, ed. D. Maoz, A. Sternberg, & E.M. Leibowitz (Dordrecht: Kluwer), p. 85
- O'Brien, P., Wilson, R., & Gondhalekar, P.M. 1988, MNRAS, 233, 801
- Osterbrock, D.E., & Pogge, R.W. 1985, ApJ, 297, 166
- Peterson, B.M., Wanders, I., Horne, K., Collier, S., Alexander, T., Kaspi, S., & Maoz, D. 1998, PASP, 110, 660
- Peterson, B.M. et al. 2000, ApJ, 542, 161
- Peterson, B.M. 2001, in *Advanced Lectures on the Starburst-AGN Connection*, eds. I. Artxaga, D. Kunth, & R.Mújica, (World Scientific), p. 3
- Pounds, K., Done, C., & Osborne, J. MNRAS, 277, L5
- Pounds, K., Edelson, R., Markowitz, A., & Vaughan, S. 2001, ApJ, 550, L15
- Puchnarewicz, E.M., Mason, K., Córdova, F., Kartje, J., Branduardi-Raymont, G., Mittaz, J., Murdin, P., & Allington-Smith, J. 1992, MNRAS, 256, 589
- Rodríguez-Pascual, P. M., Mas-Hesse, J. M., & Santos-Lleó, M. 1997a, A&A, 327, 72
- Rodríguez-Pascual, P.M. et al. 1997b, ApJ, 110, 9
- Rokaki, E., & Boisson, C. 1999, MNRAS, 307, 41
- Shields, J.C., Ferland, G.J., & Peterson, B.M. 1995, ApJ, 441, 507
- Schlegel, D.J., Finkbeiner, D.P., & Davis, M. 1998, ApJ, 500, 525
- Shemmer, O. et al. 2001, submitted to ApJ

- Turner, J. et al. 1999, in Proceedings of the 19th Texas Symposium on Relativistic Astrophysics & Cosmology, ed Paul, T. Montmerle, & E., Aubourg (Saclay: CEA), E441
- Turner, J. et al. 2001, submitted to ApJ
- Vaughan, S., Pounds, K., Reeves, J., Warwick, R., & Edelson, R. 2000, MNRAS, 308, 34
- van Groningen, E. 1993, A&A, 272, 25
- Walter, R., & Fink, H. 1993, A&A, 274, 105
- Wandel, A., & Boller, T. 1998, A&A, 331, 884
- Wandel, A., Peterson, B. M., & Malkan, M. A. 1999, ApJ, 526, 579
- Wanders, I. et al. 1997, ApJS, 113, 69
- Welsh, W., & Horne, K. 1991, ApJ, 379, 586
- Welsh, W.F., Peterson, B.M., Koratkar, A.P., & Korista, K.T. 1998, ApJ, 509, 118
- White, R.J., & Peterson, B.M. 1994, PASP, 106, 879
- Wilkes, B. 1989, MNRAS, 207, 73
- Wilkes, B., Kuraszkiewicz, J., Green, P., Mathur, S., & McDowell, J. C. 1999, ApJ, 513, 76

Fig. 1.— The observed mean (top panel) and root-mean-square (rms: bottom panel) spectra of the 46 G140L spectra. These spectra have been corrected for Galactic reddening using $E(B-V) = 0.06$ mag. The mean spectrum displays many emission and absorption-line features, and the solid line denotes the best-fit power-law continuum, see text for further details. The continuum bands used in this paper are as indicated. The rms spectrum shows evidence for Ly α $\lambda 1216$, N v $\lambda 1240$, Si iv +O iv] $\lambda 1400$, C iv $\lambda 1549$, and He ii $\lambda 1640$ variations with amplitudes of < 4, 5, 6, 5, and 4%, respectively.

Fig. 2.— The observed mean (top panel) and root-mean-square (rms: bottom panel) spectra of the 46 G230L spectra. These spectra have been corrected for Galactic reddening using $E(B-V) = 0.06$ mag. The mean spectrum displays many emission and absorption-line features. The prominent emission-lines are marked, including the continuum bands utilized in §4.1. The rms spectrum shows evidence for Si III $\lambda 1892$, C III] $\lambda 1909$, and Mg II $\lambda 2798$ variations with amplitudes of < 6, 6, and 4%, respectively.

Fig. 3.— An illustrative example of the ambiguity in the Ly α $\lambda 1216$ emission-line profile, and hence spectral line measurements (for which absorption corrections have been made) of §3, due to different interpolation schemes. The solid line histogram presents the Ly α $\lambda 1216$ emission-line profile, and the dashed and dotted histograms detail the linear and cubic spline interpolation corrections over the absorption feature.

Fig. 4.— The mean Ly α $\lambda 1216$, C IV $\lambda 1549$, and Mg II $\lambda 2798$ emission-line profiles of Figs. 1 and 2 as a function of velocity. The emission line profile amplitudes have been normalized to unity. The high ionization lines of Ly α $\lambda 1216$ and C IV $\lambda 1549$ and the low ionization line of Mg II $\lambda 2798$ do not appear notably blueshifted or redshifted relative to systemic velocities.

Fig. 5.— The 1984 Jan 17 IUE SWP observation of Akn 564. For comparison purposes, our mean G140L spectrum of Fig. 1 is overlaid as the thicker line. These spectra have been corrected for Galactic reddening using $E(B-V) = 0.06$ mag. The continuum and emission-line fluxes are in qualitative agreement.

Fig. 6.— The observed continuum light curves for the 60 day monitoring period, with mean observed wavelength as labelled. The amplitude of the intrinsic rms variations is about 6%, and they all exhibit the same qualitative behaviour.

Fig. 7.— The Akn 564 1365 \AA (solid line) and NGC 7469 (a Seyfert 1 galaxy) 1315 \AA (dotted line) autocorrelation functions (ACFs), respectively. The relative steepness of the 1365 \AA ACF (compared to the 1315 \AA ACF) indicates Akn 564’s fluctuation power density spectrum is flatter than that for NGC 7469, and thereby exhibits more power on short time scales. The full-width-half-maximum of the ACFs are 3.27 and 4.93 days for Akn 564 and NGC 7469, respectively, and are indicative of characteristic UV variability timescales.

Fig. 8.— CCFs for four UV continuum regions, mean observed wavelengths as labelled. The solid line and data points with error bars detail the ICCF and ZDCF CCFs, respectively, and are in good agreement. The 1480–3000 \AA variations are strongly correlated with those at 1365 \AA as evidenced by maximum cross-correlation coefficients of $r_{\max} \approx 0.9$. The 1480–2100 \AA variations occur quasi-simultaneously, since their CCFs all peak at about zero lag. The 3000 \AA CCF peaks at about 0.5 days.

Fig. 9.— CCFs for four optical continuum regions, nominal observed wavelengths as labelled. All CCFs have been computed with respect to the variations at 1365 Å. The solid line and data points with error bars detail the ICCF and ZDCF CCFs, respectively, and are in good agreement. The 4900–6900 Å variations are correlated with those at 1365 Å, as evidenced by maximum correlation coefficients of $r_{\max} \approx 0.5$. Moreover, they are delayed by about 2 days with respect to those at UV wavelengths.

Fig. 10.— The UV lag spectrum binned to 40 Å. Top panel: The solid histogram denotes the centroid lags. The error bars are those derived from a model-independent quasi-bootstrap and flux randomization method. The solid line represents the best-fit function $\tau \propto (\lambda^\gamma - \lambda_0^\gamma)$, with $\lambda_0 = 1365$ Å and $\gamma = 2.4 \pm 0.1$. There is a clear trend of increasing lag with wavelength. Bottom panel: The solid histogram denotes the maximum correlation coefficient. The 1150–3140 Å variations are well correlated with $r_{\max} \approx 0.9$. The dip in the maximum correlation coefficient at about 1700 Å is due to calibration uncertainties in the G230L spectra. See text for further details.

Fig. 11.— The UV/optical lag spectrum. The optical lag measurements, denoted by the open symbols, are derived from contemporaneous optical monitoring data presented in Paper III. The solid line represents the best-fit function $\tau \propto (\lambda^\gamma - \lambda_0^\gamma)$, with $\lambda_0 = 1365$ Å and $\gamma = 1.3 \pm 0.1$. The dotted line represents the best-fit function to the UV data, denoted by the solid histogram, detailed in Fig. 10, i.e., $\gamma = 2.4 \pm 0.1$. By including the optical data, the lag-wavelength relationship flattens.

Fig. 12.— Ly α λ1216 light curves for the 60 day monitoring period. The data points with error bars describe the emission-line variations between 1240–1243 Å and 1247–1250 Å and the dashed line those between 1240–1250 Å. In both cases the continuum is defined by a linear fit between 1155–1180 Å and 1350–1380 Å. The 1365 Å light curve, §4.1 and Fig. 6, is scaled and vertically shifted to fit light curve 1, and is shown by the solid line. The emission-line variations denoted by the dashed line, include any possible variable contribution from the intrinsic H I absorption feature. The intrinsic Ly α λ1216 flux amplitude variations are about 1%, and both light curves exhibit similar qualitative behaviour which in turn mimics those of the continuum regions. We note the dashed line variations have been normalized to have the same mean value as those denoted by the data points.

Fig. 13.— CCFs for the Ly α λ1216 emission-line. The solid line and filled data points represent the ICCF and ZDCF CCFs, respectively for light curve 1, and the dashed line and open data points are for light curve 2 (see Fig. 12). The Ly α λ1216 variations are correlated with the 1365 Å variations with a maximum cross-correlation amplitude $r_{\max} \approx 0.5$. Their CCFs peak away from zero at about 2 days, and the differences between them are not statistically significant.

Fig. 14.— The reverberation-based virial mass and optical luminosity relationship for AGNs. The filled circles are Seyfert galaxies from Wandel et al. (1999), and the open circles are QSOs from Kaspi et al. (2000). The large triangles are the AGNs from the same sources whose broad lines have widths less than $\sim 2000 \text{ km s}^{-1}$. Our upper limit mass estimate for Akn 564 is shown as a filled diamond. The best-fit regression line based on the narrow-line objects is denoted by the dashed line, with $M \propto L^{0.48 \pm 0.08}$.

Table 1. Emission-Line Characteristics

Line (1)	FW _{0.5} ^a (2)	F _{0.5} ^b (3)	FW _{0.2} ^a (4)	F _{0.2} ^b (5)	$\lambda_{0.2}^{\text{cen}}$ (Å) (6)
Ly α	2114	5.30	3553	6.51	1245.2
N V	2809	1.98	4725	2.56	1270.5
[O I]	788	0.15	1563	0.20	1338.1
Si IV+O IV]	3270	0.70	4859	0.84	1433.9
N IV]	928	0.35	1487	0.44	1521.6
C IV	1934	1.33	3469	1.76	1586.3
He II	1195	0.91	2585	1.38	1679.6
He II ^c	1831	1.04	3875	1.44	1682.7
N III] ^c	1882	0.56	3930	0.80	1794.0
C III] ^c	1920	0.86	—	—	—
Mg II ^c	1659	1.73	—	—	—

^aIn km s^{−1}.

^bIn 10^{−13} ergs s^{−1} cm^{−2}.

^cSpectral measurements from the G230L mean spectrum.
All other measurements from the G140L mean spectrum.

^dThe spectra are corrected for a Galactic reddening of $E(B - V) = 0.06$, and assume zero internal reddening.

Table 2. Continuum and Emission-Line Variability Characteristics

Light Curve (1)	\bar{F} ^a (2)	σ_F^a (3)	F_{var} (4)	R_{max} (5)
1365 Å	7.21	0.44	0.061	1.31
1480 Å	6.99	0.46	0.065	1.33
1640 Å	6.98	0.46	0.064	1.33
2100 Å	5.82	0.30	0.051	1.28
3000 Å	6.48	0.25	0.037	1.19
$\text{Ly}\alpha \lambda 1216^b$	16.95	0.30	0.015	1.07
$\text{Ly}\alpha \lambda 1216^c$	29.10	0.42	0.012	1.06

^aUnits are 10^{-15} erg cm $^{-2}$ s $^{-1}$ Å $^{-1}$ for continuum fluxes and 10^{-14} erg cm $^{-2}$ s $^{-1}$ for the line fluxes. All light curves have $N = 46$ data points.

^bLy α $\lambda 1216$ variations between 1240–1243 Å and 1247–1250 Å. See §5 for further details.

^cLy α $\lambda 1216$ variations between 1240–1250 Å. See §5 for further details.

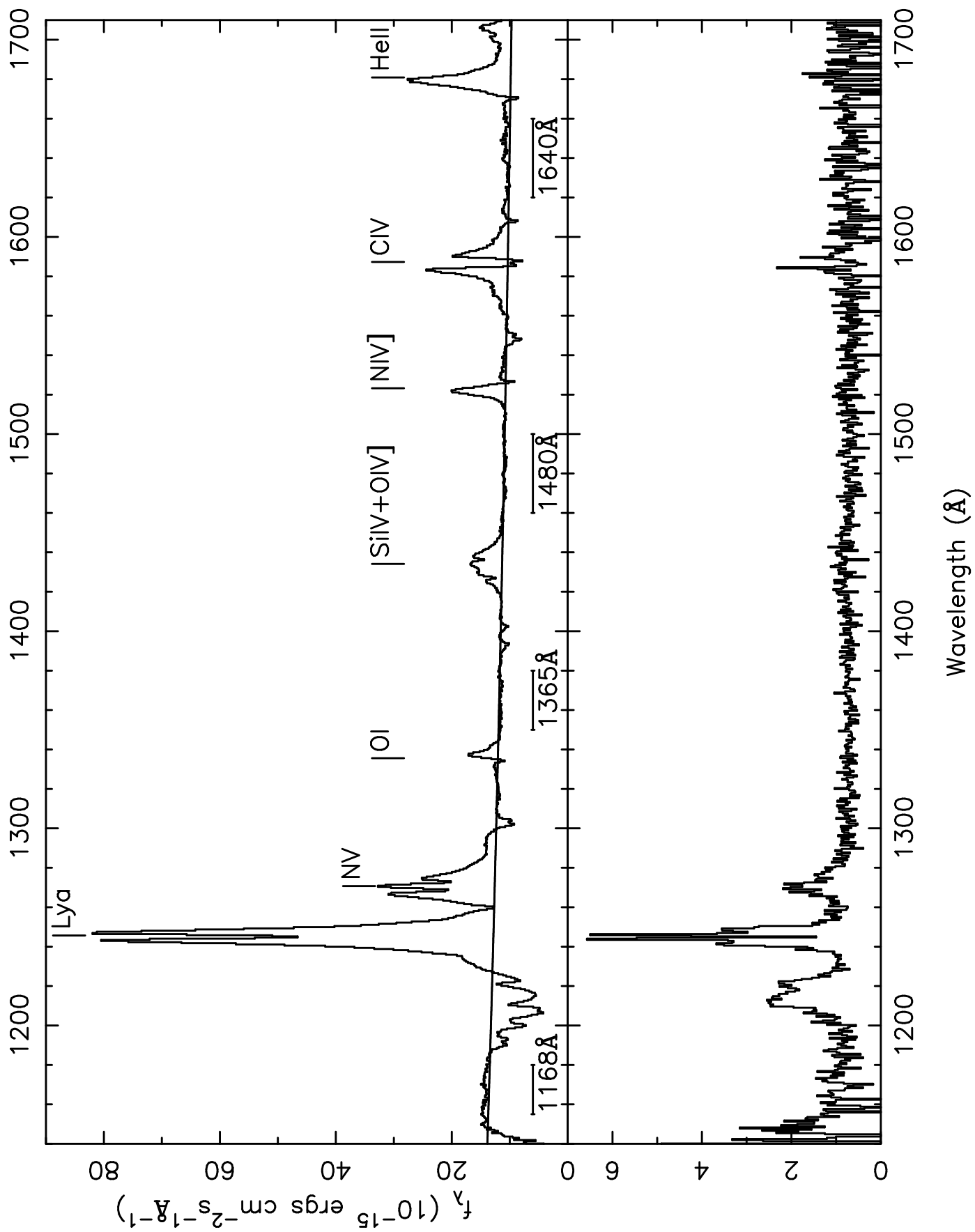
Table 3. Cross-Correlation Results

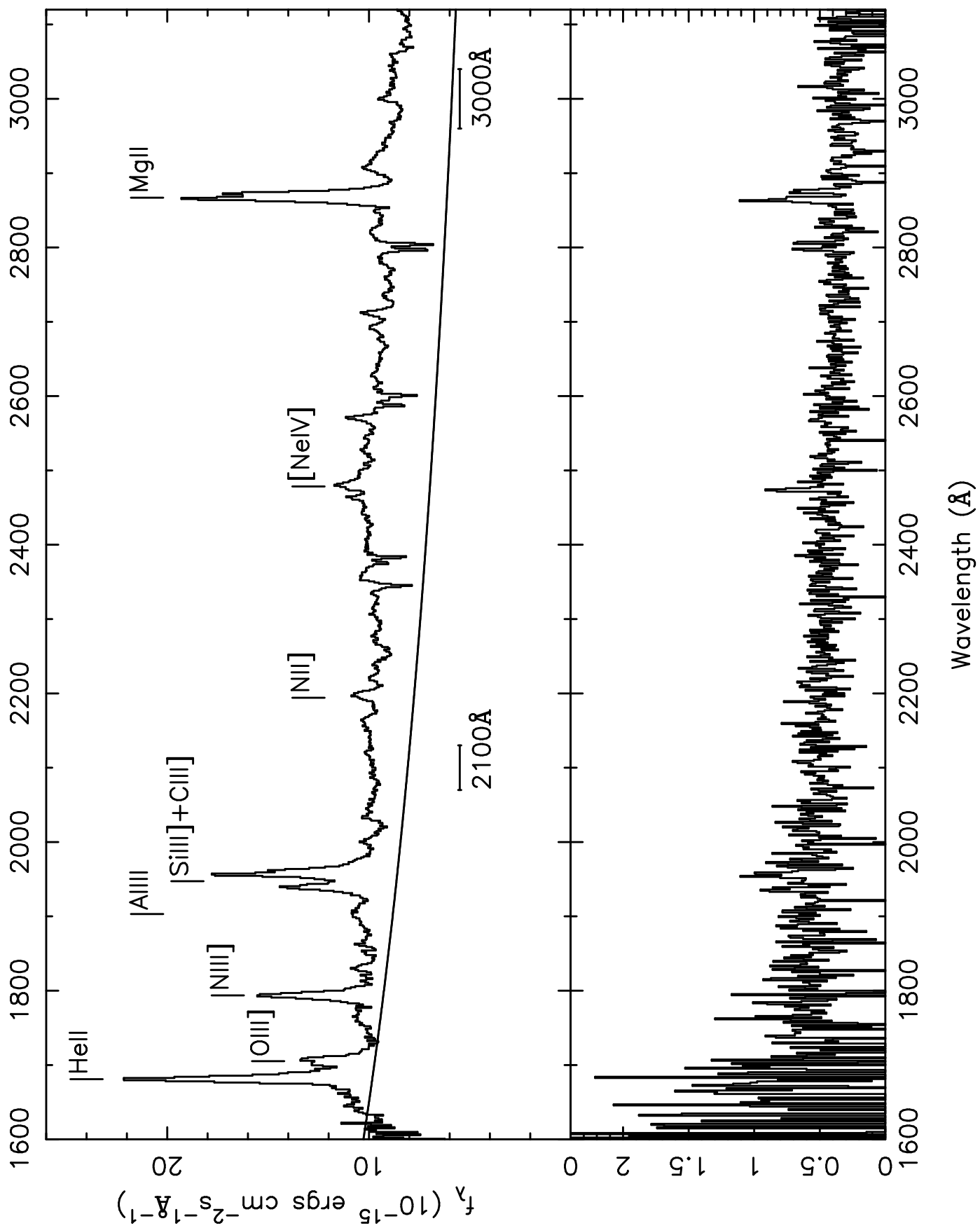
Band	τ_{cen}^a		τ_{peak}^a		r_{max}		FWHM ^a (8)
	ICCF (1)	ZDCF (2)	ICCF (4)	ZDCF (5)	ICCF (6)	ZDCF (7)	
1480Å	-0.0 ^{+0.2} _{-0.2}	0.0	0.0±0.0	0.0±0.4	1.0	1.0	3.3
1640Å	0.1 ^{+0.2} _{-0.2}	0.2	0.0±0.1	0.0±0.4	0.9	1.0	3.0
2100Å	0.3 ^{+0.4} _{-0.2}	0.3	0.3 ^{+0.2} _{-0.1}	0.0 ^{+0.4} _{-0.4}	0.9	0.9	3.0
3000Å	1.0 ^{+0.4} _{-0.3}	0.7	0.5 ^{+1.1} _{-0.0}	0.0 ^{+1.4} _{-0.4}	0.8	0.7	3.5
4900Å	1.8 ^{+0.5} _{-0.4}	1.8	2.2 ^{+0.2} _{-1.0}	2.7±1.3	0.7	0.6	3.6
5200Å	1.8 ^{+0.6} _{-0.4}	1.7	1.4 ^{+1.0} _{-0.1}	1.7 ^{+2.5} _{-1.0}	0.6	0.5	3.7
6600Å	2.2 ^{+1.7} _{-8.3}	2.3	2.5 ^{+1.8} _{-8.8}	2.1 ^{+0.8} _{-1.5}	0.4	0.5	3.8
6900Å	2.6 ^{+1.6} _{-5.1}	2.4	3.0 ^{+1.8} _{-6.4}	2.7 ^{+1.3} _{-1.8}	0.4	0.3	3.7
$\text{Ly}\alpha \lambda 1216^b$	0.9 ^{+0.4} _{-1.2}	0.4	0.7 ^{+0.6} _{-1.1}	1.0 ^{+0.6} _{-1.7}	0.6	0.5	5.0
$\text{Ly}\alpha \lambda 1216^c$	2.8 ^{+0.0} _{-2.3}	1.9	2.7 ^{+0.0} _{-2.2}	1.0 ^{+1.8} _{-1.4}	0.5	0.4	3.6

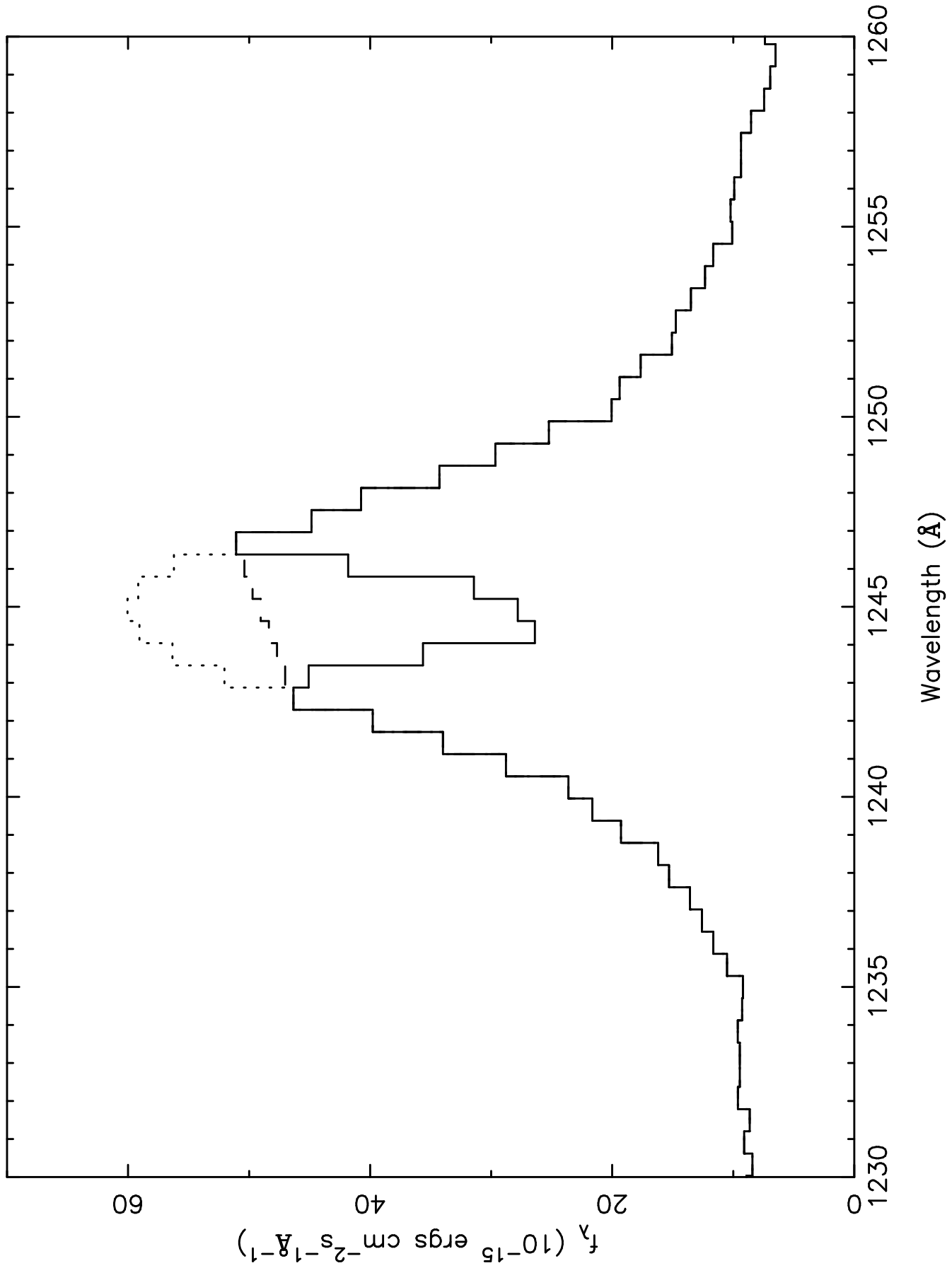
^aIn days.

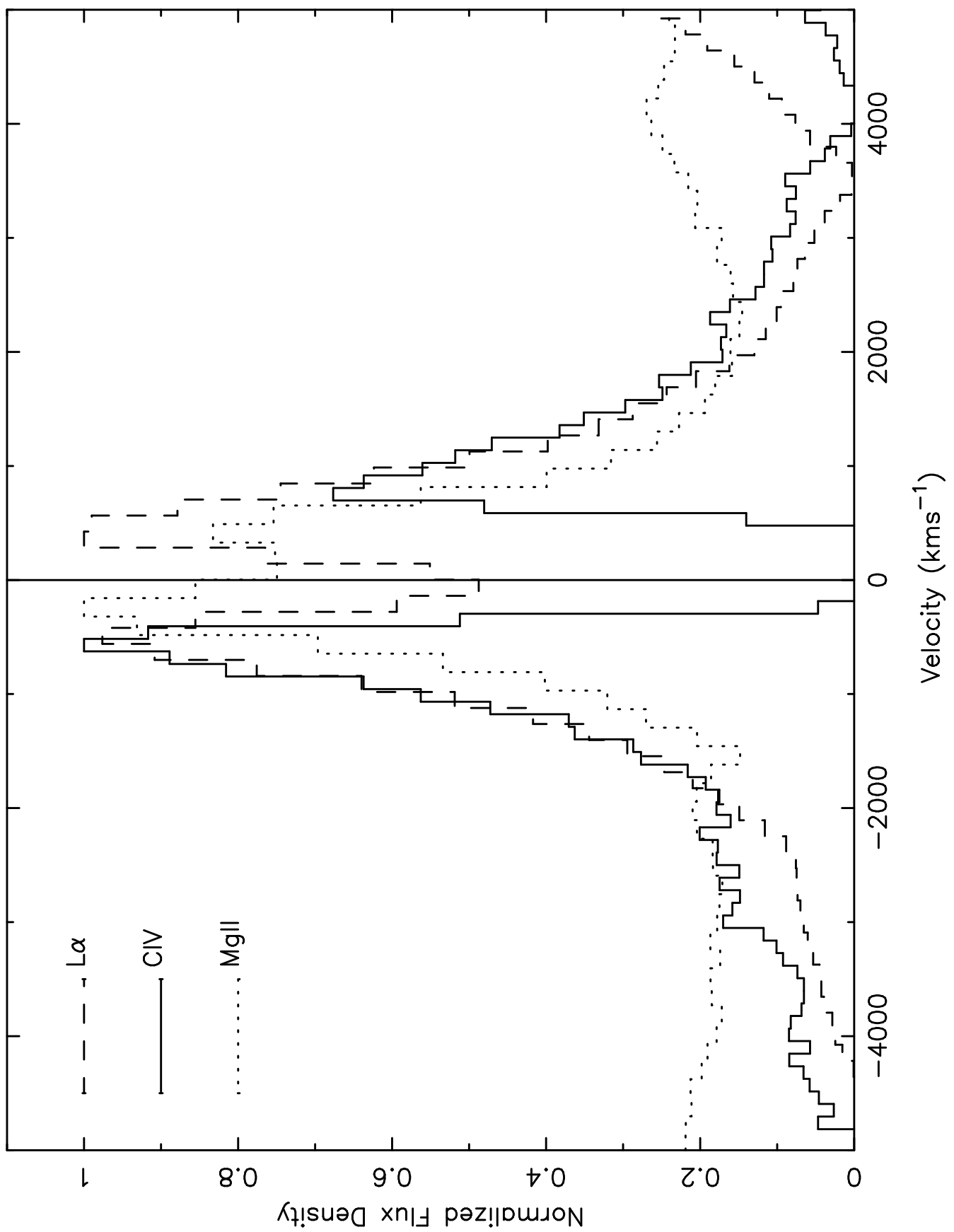
^b $\text{Ly}\alpha \lambda 1216$ variations between 1240-1243Å and 1247-1250Å. See §5 for further details.

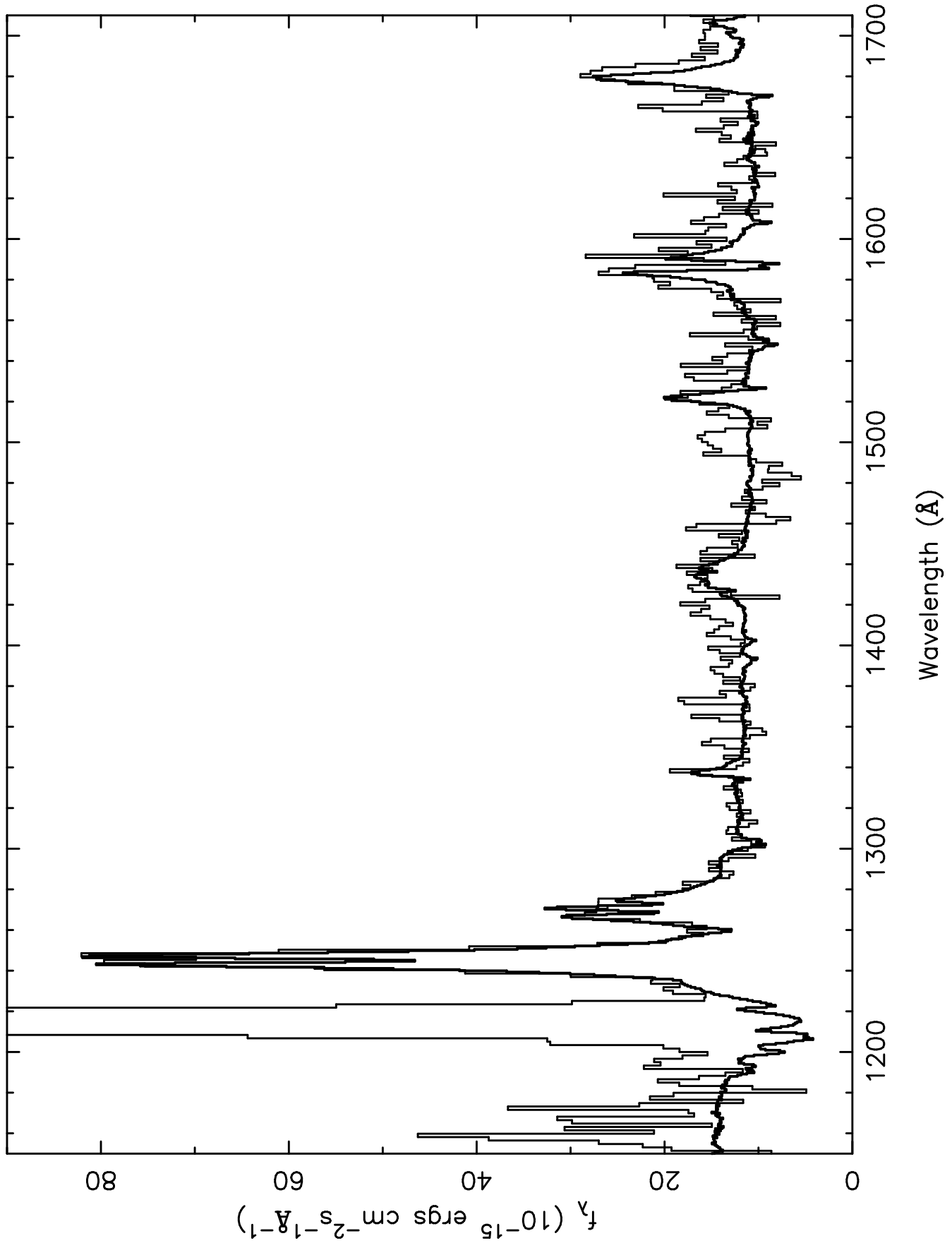
^c $\text{Ly}\alpha \lambda 1216$ variations between 1240-1250Å. See §5 for further details.

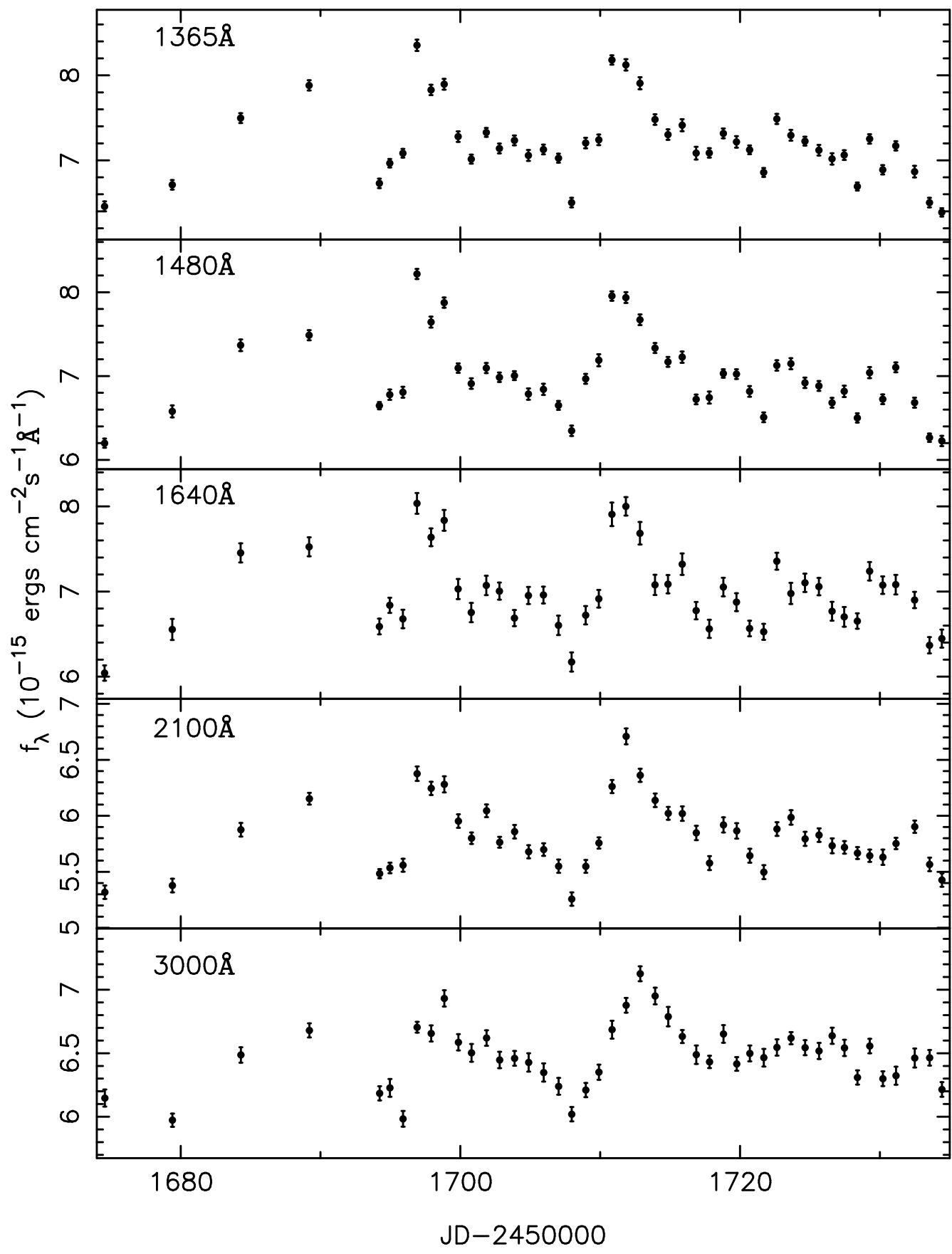


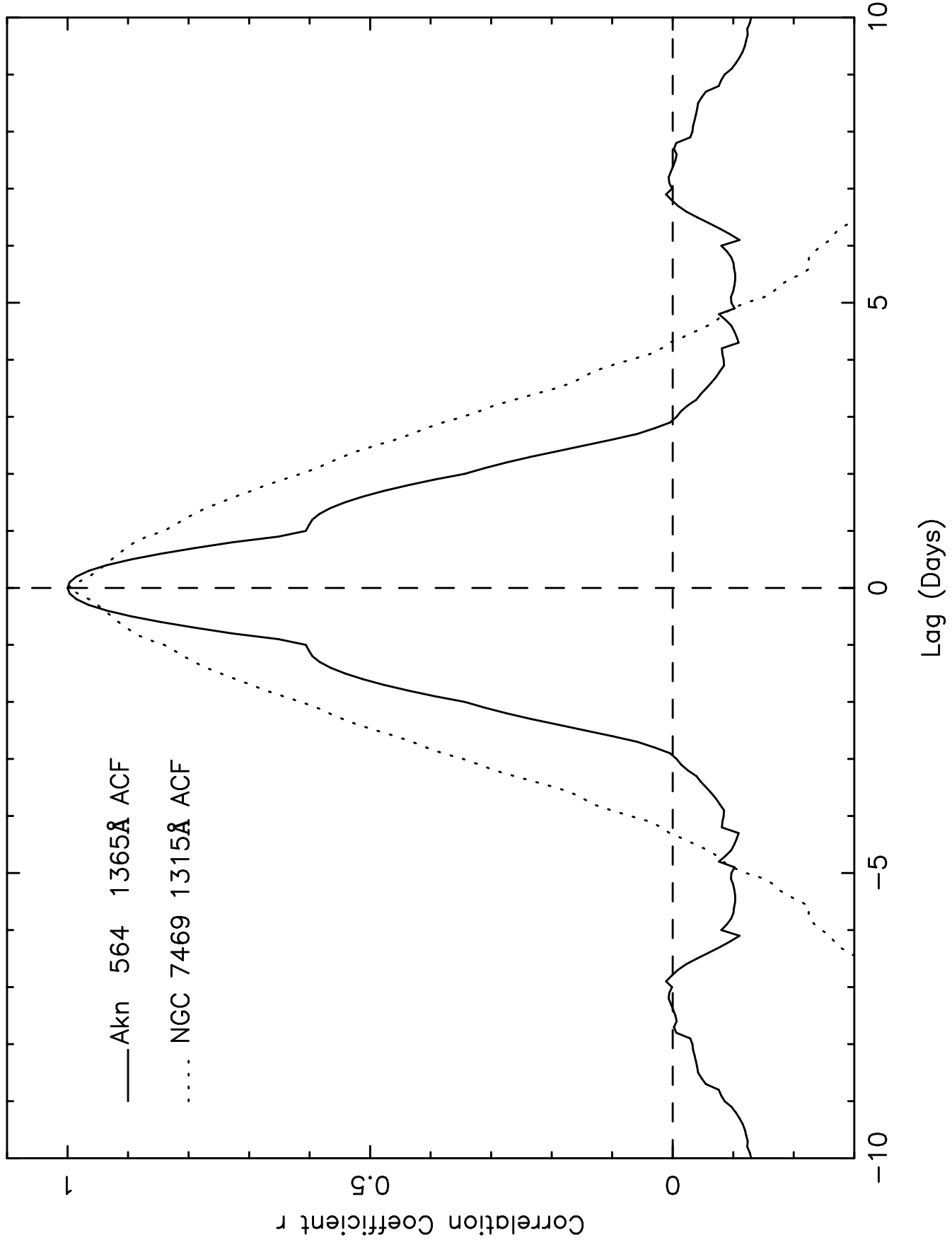


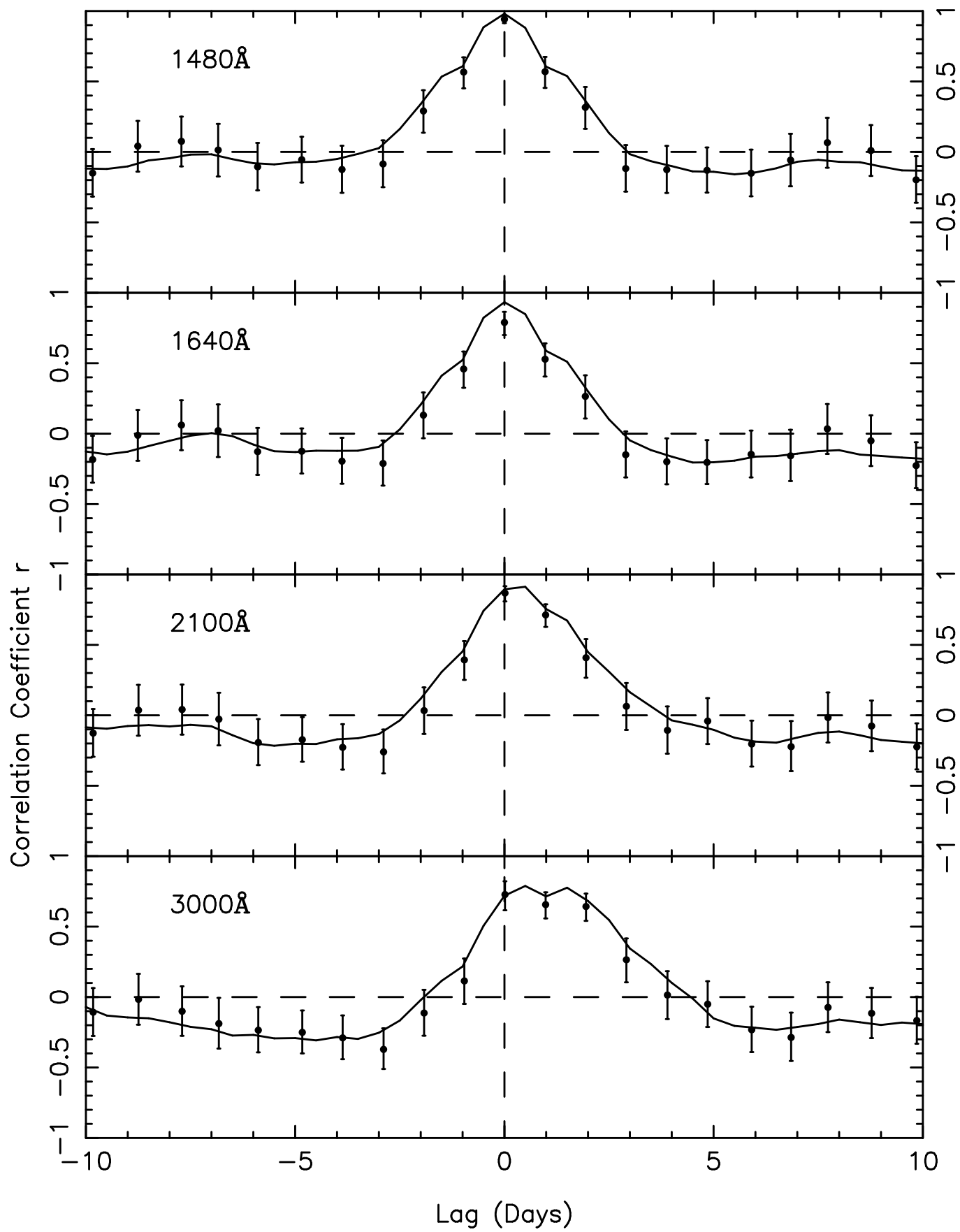


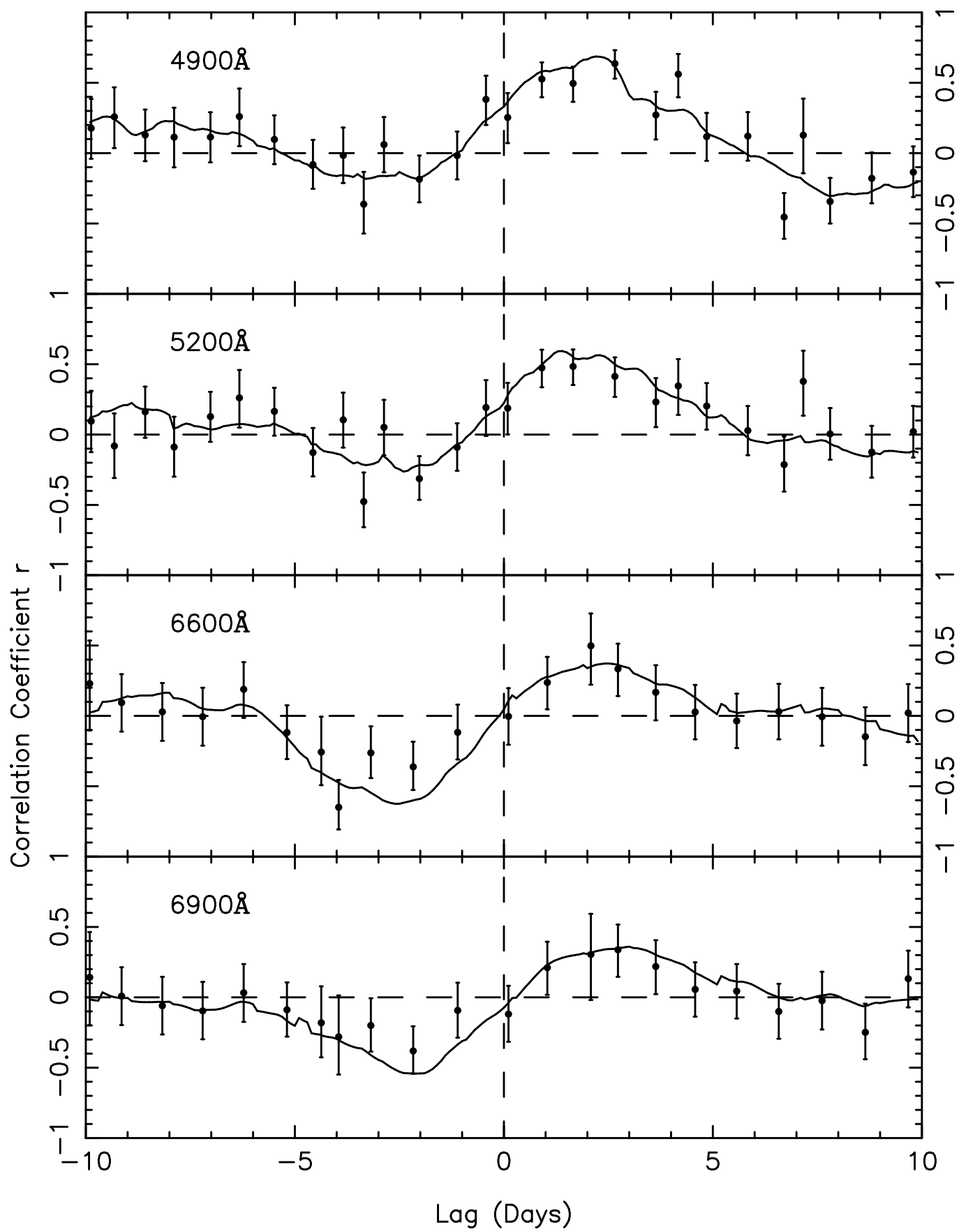


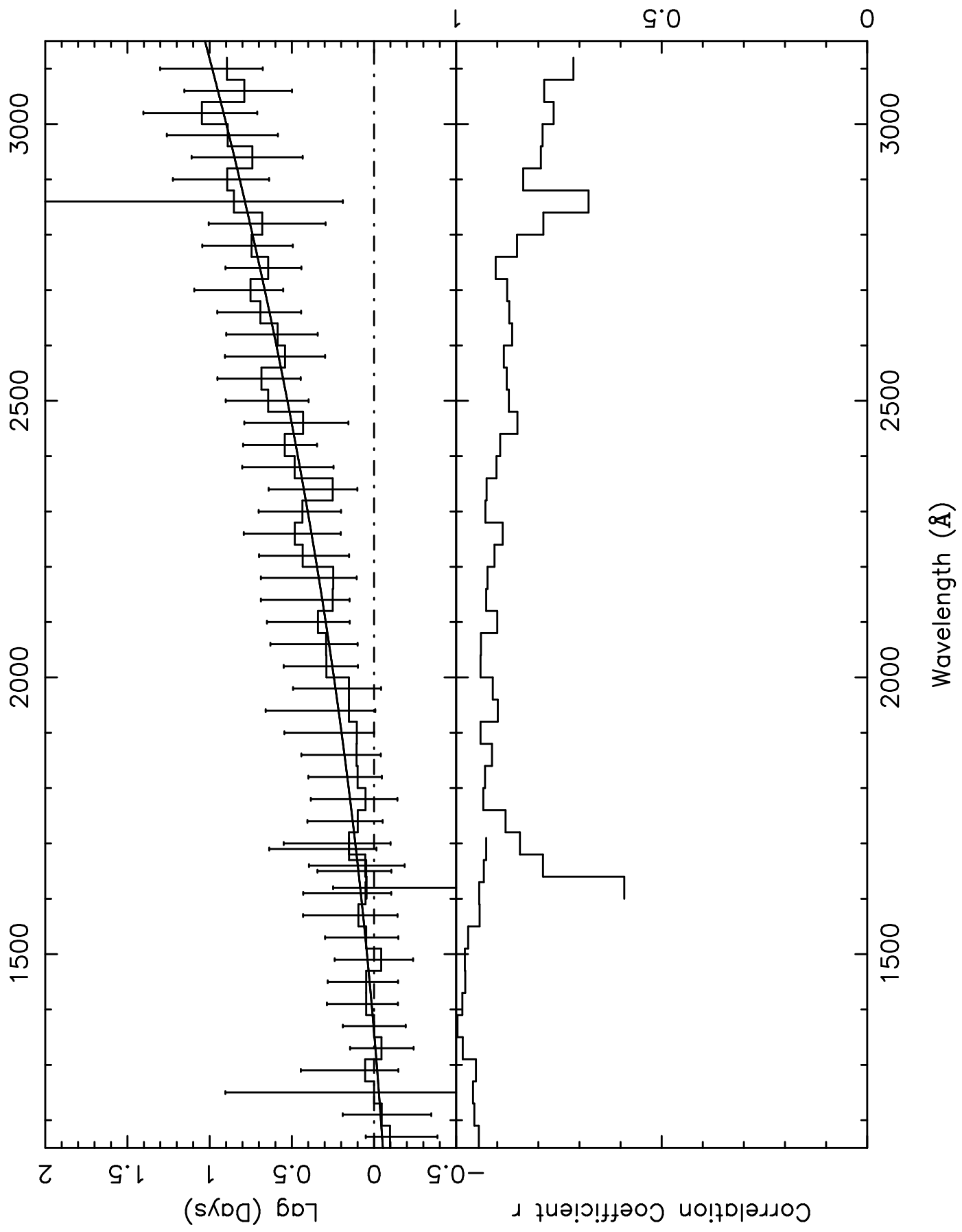


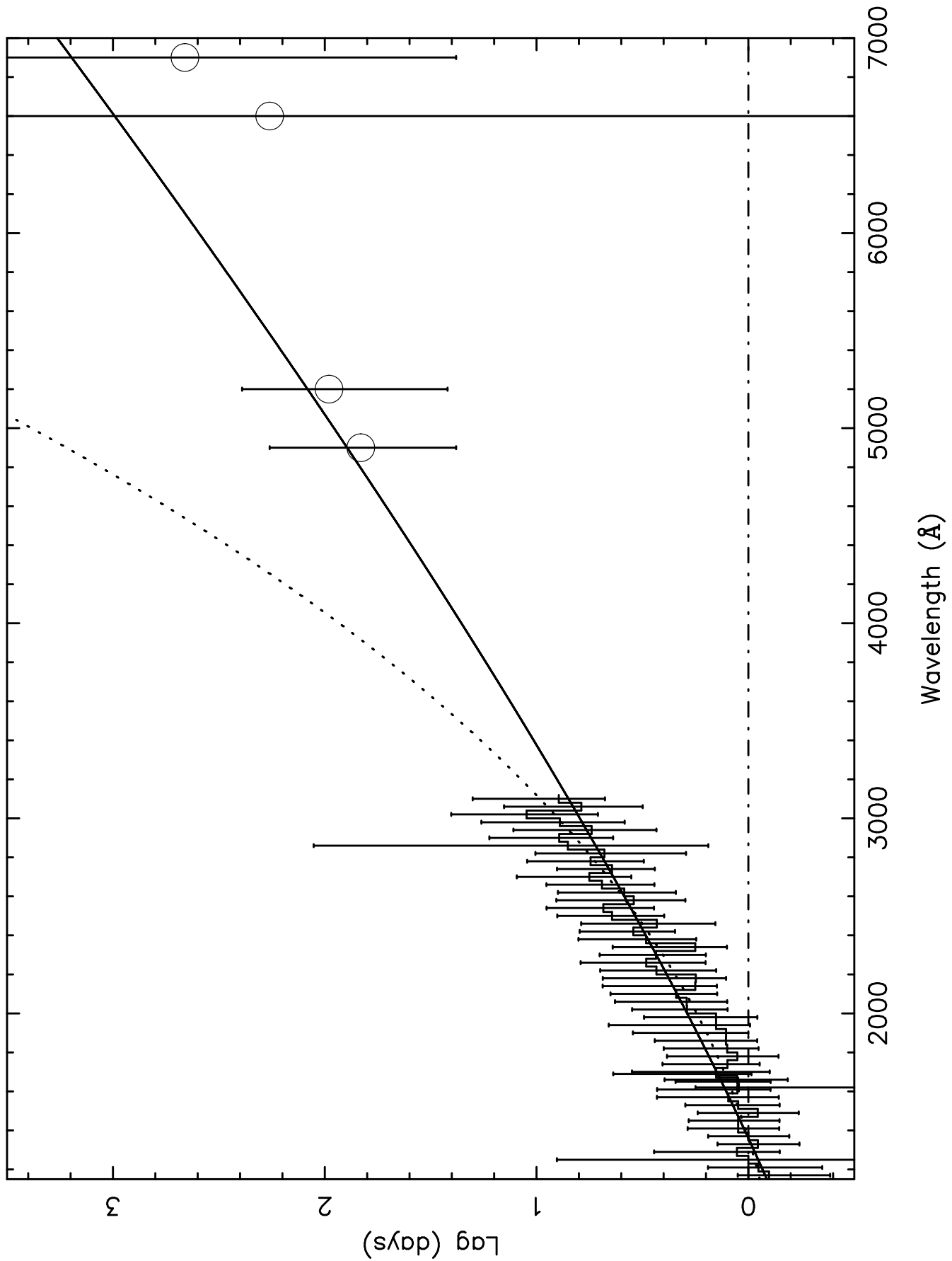


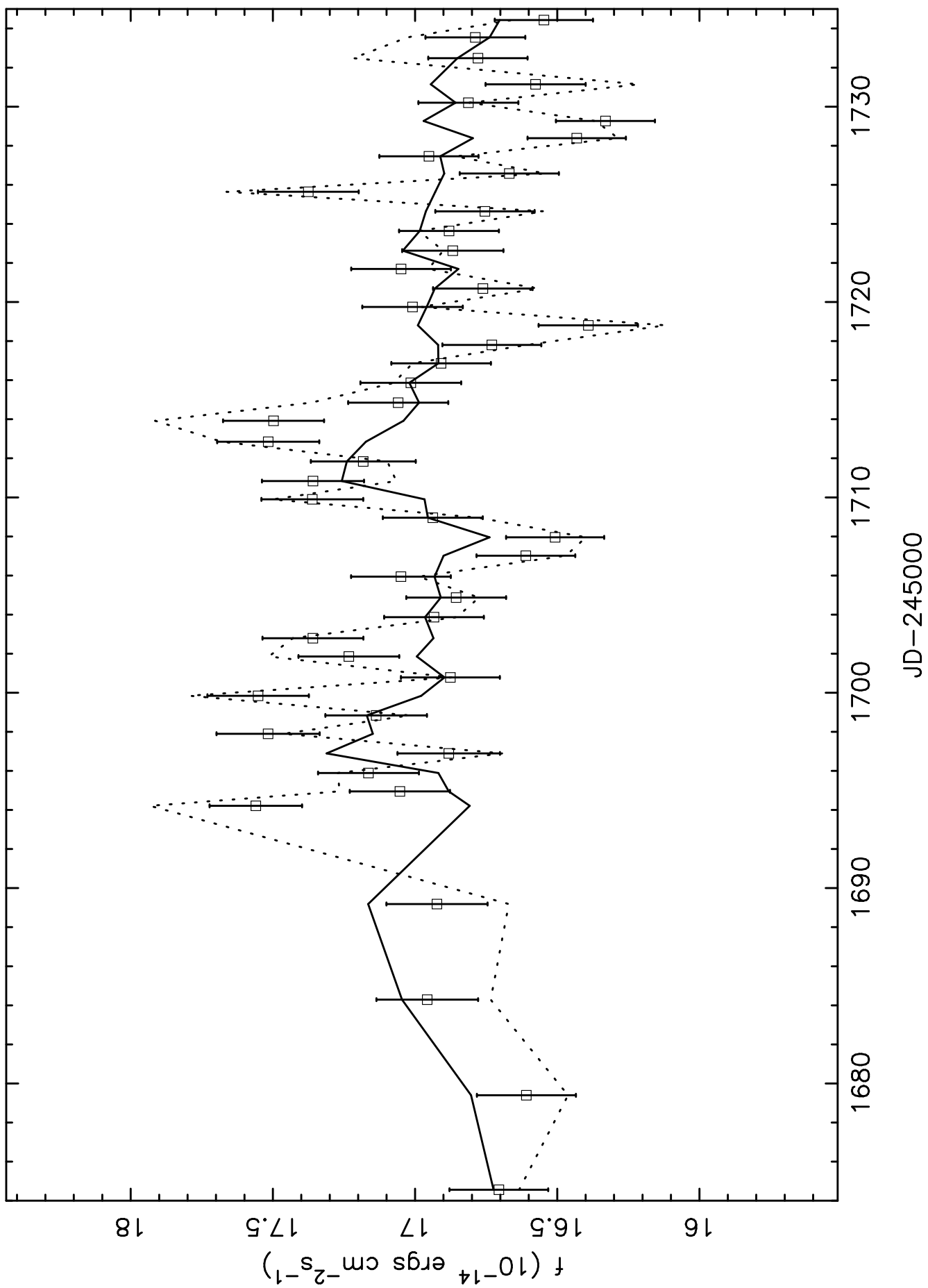


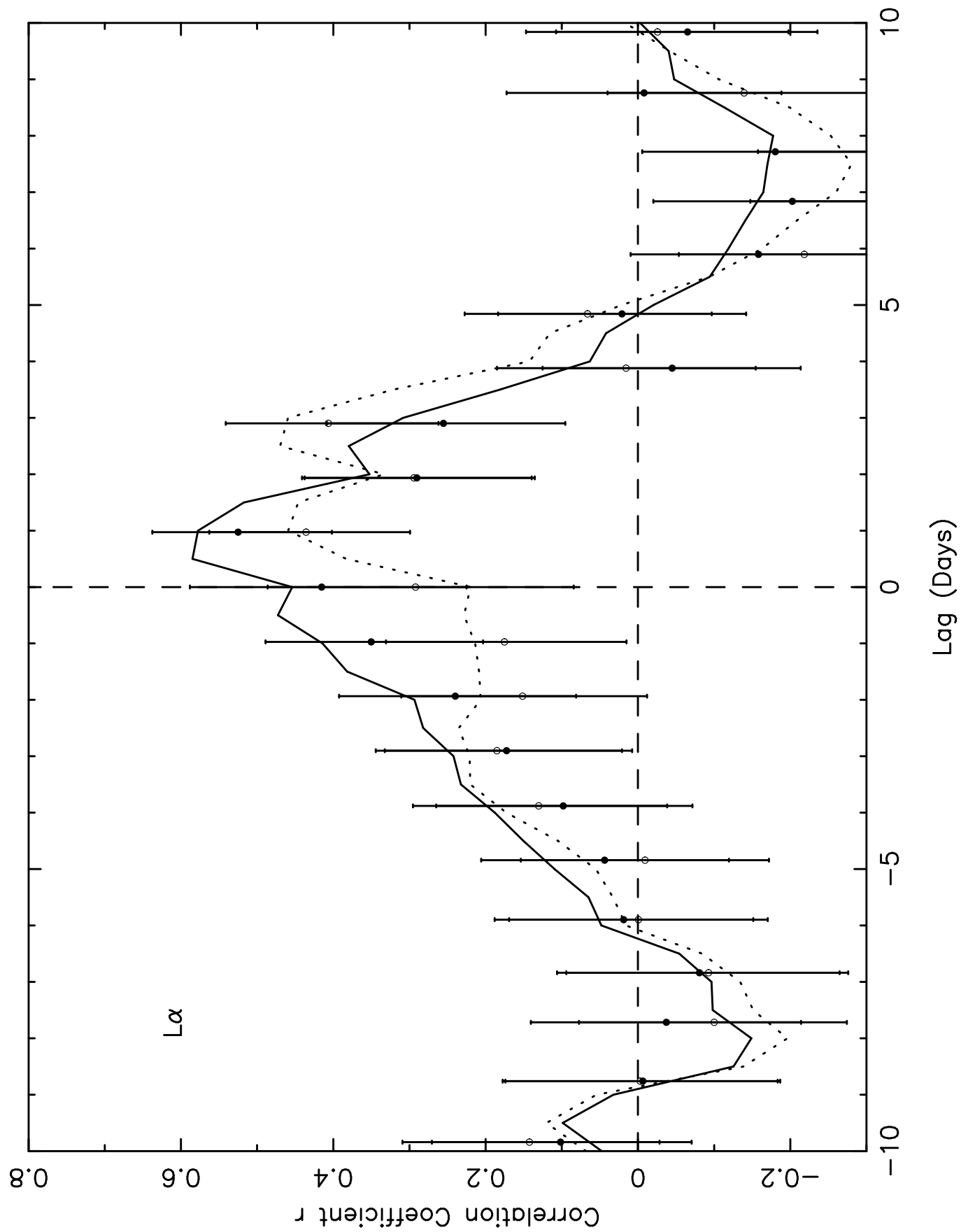












M (solar masses)

